City Research Online

City, University of London Institutional Repository

Citation: Coombs, W.M. & Crouch, R.S. (2011). Algorithmic issues for three-invariant hyperplastic Critical State models. Computer Methods in Applied Mechanics and Engineering, 200(25-28), pp. 2297-2318. doi: 10.1016/j.cma.2011.03.019

This is the accepted version of the paper.

This version of the publication may differ from the final published version.

Permanent repository link: https://openaccess.city.ac.uk/id/eprint/15546/

Link to published version: https://doi.org/10.1016/j.cma.2011.03.019

Copyright: City Research Online aims to make research outputs of City, University of London available to a wider audience. Copyright and Moral Rights remain with the author(s) and/or copyright holders. URLs from City Research Online may be freely distributed and linked to.

Reuse: Copies of full items can be used for personal research or study, educational, or not-for-profit purposes without prior permission or charge. Provided that the authors, title and full bibliographic details are credited, a hyperlink and/or URL is given for the original metadata page and the content is not changed in any way.

City Research Online: http://openaccess.city.ac.uk/ publications@city.ac.uk

Algorithmic issues for three-invariant hyperplastic Critical State models

William M. Coombs, Roger S. Crouch *

Durham University, School of Engineering and Computing Sciences, South Road, Durham DH1 3LE, United Kingdom

A B S T R A C T

Implicit stress integration and the consistent tangents are presented for Critical State hyperplasticity models which include a dependence on the third invariant of stress. An elliptical deviatoric yielding criterion [43] is incorporated within the family of geotechnical models first proposed by Collins and Hilder [8]. An alternative expression for the yield function is proposed and the consequences of different forms of that function are revealed in terms of the stability and efficiency of the stress return algorithm. Errors associated with the integration scheme are presented. It is shown how calibration of the two new material constants is achieved through examining one-dimesional consolidation tests and undrained triaxial compression data. Material point simulations of drained triaxial compression tests are then compared with established experimental results. Strain probe analyses are used to demonstrate the concepts of energy dissipation and stored plastic work along with the robustness of the integration method. Over twenty finite element boundary value problems are then simulated. These include single three-dimensional element tests, plane strain footing analyses and cavity expansion tests. The rapid convergence of the global Newton–Raphson procedure using the consistent tangent is demonstrated in small strain and finite deformation simulations.

1. Introduction

Following on from the pioneering work of Ziegler [45], Houlsby [26] and Collins and Houlsby [6], a number of constitutive models based on a hyperplasticity framework have been constructed for geomaterials [7–14,28,29,35,36]. These offer improvements over conventional plasticity formulations which can fail to satisfy fundamental thermodynamic principles. Hyperplasticity establishes the constitutive model using just two scalar functions; the free-energy function and the dissipation function. Curiously, despite their attraction, very few hyperplasticity models have been incorporated and tested in generalised numerical analysis schemes such as the finite element method. In particular, to date, the consistent linearisation (stress integration and algorithmic tangent) for the isotropic family of non-linearly hardening constitutive models proposed by Collins and Hilder [8] (further developed by Collins et al. [9–11,13]) has yet to be presented. These formulations embrace the condition, known as the Critical State [38], whereby unbounded plastic distortions take place with no change in state (constant stress and volume). Here we provide the linearisation and illustrate the performance of these extended models using both material point and boundary value simulations. The work will be of particular interest to those simulating the compactive-dilative inelastic response of granular material.

The paper is organised as follows. Section 2 presents the constitutive formulation, including (i) the hyperelastic relationship, (ii) the plasticity relations, (iii) the introduction of the Willam–Warnke (W–W) [43] Lode angle dependency (LAD) within the hyperplastic framework and (iv) calibration of the non-classical material parameters. Here we make use of a different means of introducing a LAD (compared to Collins and Hilder [8]) in order to overcome previous limitations. Application of the backward Euler (BE) stress integration for these models is thoroughly described in Section 3 together with an assessment of the magnitude of the errors associated with the stress return. Derivation of the consistent algorithmic tangent is presented in Section 4. Numerical simulations are reported in Section 5 for material point tests and for over twenty finite element simulations (i) a simple single 3D element test (ii) numerical verification through a plane strain flexible footing comparison with Borja and Tamagnini [3] (iii) a plane strain smooth rigid footing problem and (iv) finite deformation cylindrical cavity expansion.

The majority of the relations given in this paper are expressed using principal stresses. In all that follows $\{\cdot\}$ and $[\cdot]$ denote 3 by 1 vectors and 3 by 3 matrices, respectively and $\{\cdot\}^T$ denotes a vector transpose. $\{\hat{\cdot}\}$ and $[\hat{\cdot}]$ are used to indicate six-component vectors and matrices respectively. We use the standard notation where $(\cdot)_{,x}$ and $(\cdot)_{,xx}$ express the first and second derivatives of $(\cdot)$ with respect to x. In line with geotechnical convention, compressive stresses are positively valued. Here the principal stresses are ordered such that σ_1 is the most tensile, while σ_3 is the most compressive.

All stresses are treated as effective stresses although the standard prime notation will be omitted. For compactness, Section 2, adopts tensor subscript notation whereas Sections 2.1 onwards use matrix and vector notation.

2. Hyperplastic constitutive formulation

The fundamental assumption for hyperplastic formulations is that the constitutive equations can be derived from a free-energy function and a dissipation function. Once these have been specified, the stress–elastic strain law, yield function and flow rule can all be obtained without the requirement for any additional assumptions. Textbook accounts of the thermomechanics of materials can be found in the volumes by Ziegler [45] and Maugin [33], amongst others. The following introduction (up to Section 2.1) draws heavily from the work of Collins et al. [6–14]. The rate of work done per unit volume is given by

$$\sigma_{ij}\dot{\varepsilon}_{ij} = \dot{\Psi} + \dot{\Phi}, \tag{1}$$

where Ψ denotes the free-energy function and $\dot{\Phi}$ identifies the dissipation rate. Both the free-energy function and dissipation rate are defined per unit volume. σ_{ij} represents the stress tensor and $\dot{\varepsilon}_{ij}$ the total strain rate tensor.

The free energy function is typically defined in terms of the total, ε_{ij}, and plastic, $\varepsilon^{\mathrm{p}}_{ij}$, strains [6]. However, here we limit ourselves to the case of *de-coupled materials* where Ψ (and its associated rate) can be split into two components: one in terms of the elastic strains and the other in terms of the plastic strains

$$\Psi = \Psi_1(\varepsilon^{\mathrm{e}}_{ij}) + \Psi_2(\varepsilon^{\mathrm{p}}_{ij}) \quad \text{and} \quad \dot{\Psi} = \left(\frac{\partial \Psi_1}{\partial \varepsilon^{\mathrm{e}}_{ij}}\right)\dot{\varepsilon}^{\mathrm{e}}_{ij} + \left(\frac{\partial \Psi_2}{\partial \varepsilon^{\mathrm{p}}_{ij}}\right)\dot{\varepsilon}^{\mathrm{p}}_{ij}. \tag{2}$$

The first term gives the true stresses in terms of the elastic strains

$$\sigma_{ij} = \frac{\partial \Psi_1}{\partial \varepsilon^{\mathrm{e}}_{ij}}, \tag{3}$$

whereas the second term in $(2)_2$ provides the *shift stress*

$$\chi_{ij} = \frac{\partial \Psi_2}{\partial \varepsilon^{\mathrm{p}}_{ij}}. \tag{4}$$

This identifies the *centre* of the yield surface in true stress space. Through these shift stresses, the second component of the free-energy function describes the kinematic hardening of the yield surface. Isotropic hardening is controlled by the dissipation rate. That rate depends on the plastic strain rate in addition to the total strains, $\dot{\Phi}(\varepsilon_{ij}, \dot{\varepsilon}^{\mathrm{p}}_{ij}, \dot{\varepsilon}^{\mathrm{p}}_{ij})$. It cannot depend on the total strain rate, otherwise purely elastic deformation would result in dissipation. For inviscid elasto-plasticity models, the dissipation rate is homogeneous of degree one in the plastic strain rates [7], giving

$$\dot{\Phi} = \frac{\partial(\dot{\Phi})}{\partial(\dot{\varepsilon}^{\mathrm{p}}_{ij})}\dot{\varepsilon}^{\mathrm{p}}_{ij}. \tag{5}$$

For frictional materials the dissipation rate depends on the total volumetric strain (or the effective pressure) but (5) remains unchanged. Using the dissipation rate we can define a *dissipative stress space*

$$\varphi_{ij} = \frac{\partial(\dot{\Phi})}{\partial(\dot{\varepsilon}^{\mathrm{p}}_{ij})}, \tag{6}$$

thus (5) becomes

$$\dot{\Phi} = \varphi_{ij}\dot{\varepsilon}^{\mathrm{p}}_{ij}. \tag{7}$$

The dissipative stress is linked to true stress through the shift stress, χ_{ij}. Substituting $(2)_2$ and (7) into (1), we obtain

$$\sigma_{ij}\dot{\varepsilon}_{ij} = \left(\frac{\partial \Psi_1}{\partial \varepsilon^{\mathrm{e}}_{ij}}\dot{\varepsilon}^{\mathrm{e}}_{ij} + \frac{\partial \Psi_2}{\partial \varepsilon^{\mathrm{p}}_{ij}}\dot{\varepsilon}^{\mathrm{p}}_{ij}\right) + \varphi_{ij}\dot{\varepsilon}^{\mathrm{p}}_{ij}. \tag{8}$$

Using (3) and (4), (8) becomes

$$\sigma_{ij}\dot{\varepsilon}_{ij} = \sigma_{ij}\dot{\varepsilon}^{\mathrm{e}}_{ij} + \left(\chi_{ij} + \varphi_{ij}\right)\dot{\varepsilon}^{\mathrm{p}}_{ij}, \tag{9}$$

which, due to the additive decomposition of the strain rate $\varepsilon_{ij} = \varepsilon^{\mathrm{e}}_{ij} + \varepsilon^{\mathrm{p}}_{ij}$, provides the following relationship between total, shift and dissipative stresses

$$\sigma_{ij} = \chi_{ij} + \varphi_{ij}. \tag{10}$$

The dissipation rate is not equal to the plastic work rate. The latter is given by the product of the true stress with plastic strain rate

$$\dot{W}^{\mathrm{p}} = \sigma_{ij}\dot{\varepsilon}^{\mathrm{p}}_{ij} = \dot{\Phi} + \chi_{ij}\dot{\varepsilon}^{\mathrm{p}}_{ij}. \tag{11}$$

Due to the constraints imposed by the second law of thermodynamics, $\dot{\Phi}$ must always be greater or equal to zero, but there is no restriction on the sign of $\dot{W}^{\mathrm{p}}$. The last term in (11) indicates the plastic work associated with the recoverable elastic deformations arising from plastic strains when grains are *locked* in position within the material fabric [12]. The concepts of dissipated and stored plastic work can be appreciated using the one-dimensional kinematically hardening model in Fig. 1(i). This rheological analogue comprises a spring (a) which is in parallel with a second spring and slider (b). In the example plot, the system is subjected to an increasing total stress, σ, followed by unloading until $\sigma_b = 0$; Fig. 1(ii). The components of stored and dissipated plastic work

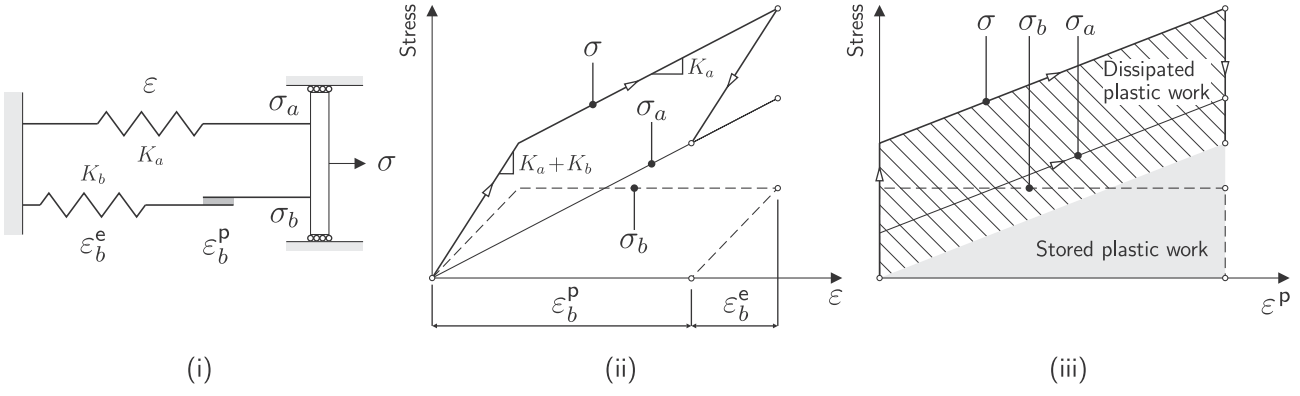

Fig. 1. (i) Rheological model of a one dimensional kinematic hardening elasto-plastic system (after Collins [12]) (ii) stress-total strain response (iii) stress-plastic strain response.

can be seen in Fig. 1(iii). Plastic dissipation occurs in the slider. Stored plastic work is a consequence of the frozen elastic energy in spring (a) which is restrained by the plastic slider.

It can be shown that the plastic strain increment is given by a normal flow rule in *dissipative stress space* [6]. This only implies an associated model in *true stress space* under the condition that the dissipation rate is independent of the true stress, σ_{ij}. For this case, when the free-energy function only depends on the elastic strains, the shift stresses are zero and the true and dissipative stress spaces are identical.

2.1. Hyperelastic relationship

Particulate geomaterials typically demonstrate a dependence of the elastic bulk modulus on the current effective pressure, or equivalently on the current elastic volumetric strain. One common approach [21] is to specify the elastic shear modulus directly from the bulk modulus assuming a constant Poisson's ratio. However, this leads to a non-linear elasticity model in which energy can be generated from certain loading cycles [3,27,46]. Here we use a variable bulk modulus with a constant shear modulus [27]. This can be realised by adopting an elastic free-energy function of the form

$$\Psi_1 = \kappa p_r \exp\left(\frac{\varepsilon_v^e - \varepsilon_{v0}^e}{\kappa}\right) + G\left(\{\gamma^e\}^T\{\gamma^e\}\right) \quad \left(\text{with } \varepsilon_v^e = \text{tr}[\varepsilon^e] \quad \text{and } \{\gamma^e\} = \{\varepsilon^e\} - \frac{\varepsilon_v^e}{3}\{1\}\right), \tag{12}$$

where κ is the elastic compressibility index, G is the shear modulus, p_r is the reference pressure, ε_{v0}^e is the elastic volumetric strain at that reference pressure and $\{1\} = \{1 \quad 1 \quad 1\}^T$. The true stress is given by the first derivative of (12) with respect to elastic strain

$$\{\sigma\} = \{\Psi_{1,\varepsilon^e}\} = p_r \exp\left(\frac{\varepsilon_v^e - \varepsilon_{v0}^e}{\kappa}\right)\{1\} + 2G\{\gamma^e\}. \tag{13}$$

The principal non-linear elastic stiffness matrix is obtained from the second derivative of (12) with respect to elastic strain

$$[D^e] = [\Psi_{1,\varepsilon^e\varepsilon^e}] = \left(K - \frac{2G}{3}\right)\{1\}\{1\}^T + 2G[I], \quad \text{where } K = \frac{p_r}{\kappa}\exp\left(\frac{\varepsilon_v^e - \varepsilon_{v0}^e}{\kappa}\right) \tag{14}$$

and $[I]$ is the third order identity matrix. The six-component elastic compliance matrix is giving by

$$\left[\widehat{C}^e\right] = \left[\widehat{D}^e\right]^{-1} = \begin{bmatrix} [C^e] & [0] \\ [0] & G^{-1}[I] \end{bmatrix}$$

$$\text{where } [C^e] = \frac{1}{9}\left(\frac{1}{K} - \frac{3G}{2}\right)\{1\}\{1\}^T + \frac{1}{2G}[I] \tag{15}$$

and [0] is the 3 by 3 null matrix.

2.2. Plasticity relations

As proposed by Collins and Hilder [8], a *two-parameter* family of Critical State [38] models can be defined using the following dissipation function

$$\dot{\Phi} = \sqrt{\left(\dot{\varepsilon}_v^p A\right)^2 + \left(\dot{\varepsilon}_\gamma^p B\right)^2}, \quad \text{where}$$

$$A = (1-\gamma)p + \frac{\gamma}{2}p_c \quad \text{and } B = M\left((1-\alpha)p + \frac{\alpha\gamma}{2}p_c\right). \tag{16}$$

The weight parameters $\alpha, \gamma \in [0,1]$ influence the shape of the yield surface (as shown in Fig. 2) and the degree of non-association of the plastic flow direction. $p = \text{tr}([\sigma])/3$ is the mean pressure and p_c defines the size of the yield surface. M is the stress ratio at which constant volume plastic shearing occurs (geometrically, this is the gradient of the Critical State line in p–q space, see Fig. 3(i)). The plastic strain invariants are defined as follows

$$\varepsilon_v^p = \text{tr}[\varepsilon^p] \quad \text{and } \varepsilon_\gamma^p = \sqrt{\{\gamma^p\}^T\{\gamma^p\}}, \quad \text{with } \{\gamma^p\} = \{\varepsilon^p\} - \frac{\varepsilon_v^p}{3}\{1\}. \tag{17}$$

The deviatoric stress invariant, q, is similarly given by

$$q = \sqrt{\{s\}^T\{s\}}, \quad \text{with } \{s\} = \{\sigma\} - p\{1\}. \tag{18}$$

Note that this q $(18)_1$ differs from that often used when describing the triaxial tests of soils (there $q = (\sigma_3 - \sigma_1)$). Assuming a free-energy function of the form [6]

$$\Psi = \Psi_1(\{\varepsilon^e\}) + \Psi_2(\{\varepsilon^p\}), \quad \Psi_2(\{\varepsilon^p\}) = \frac{\gamma(\lambda-\kappa)}{2}p_r \exp\left(\frac{\varepsilon_v^p}{\lambda-\kappa}\right), \tag{19}$$

with Ψ_1 given by (12), we can define the shift stress as

$$\{\chi\} = \frac{\gamma p_c}{2}\{1\}, \quad \text{with } p_c = p_r \exp\left(\frac{\varepsilon_v^p}{\lambda-\kappa}\right). \tag{20}$$

Moving between dissipative and true stress space corresponds to a (pressure dependent) hydrostatic shifting of the yield surface. The

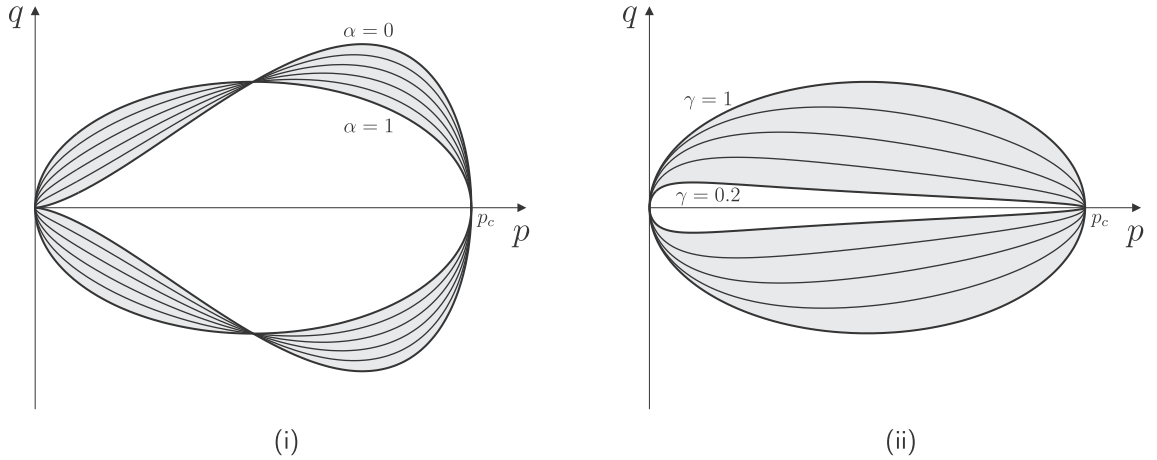

Fig. 2. Yield surfaces for the two-parameter Critical State hyperplastic models: (i) $\alpha \in [0,1]$ with $\gamma = 1$ (ii) $\gamma \in [0.2,1]$ with $\alpha = 1$.

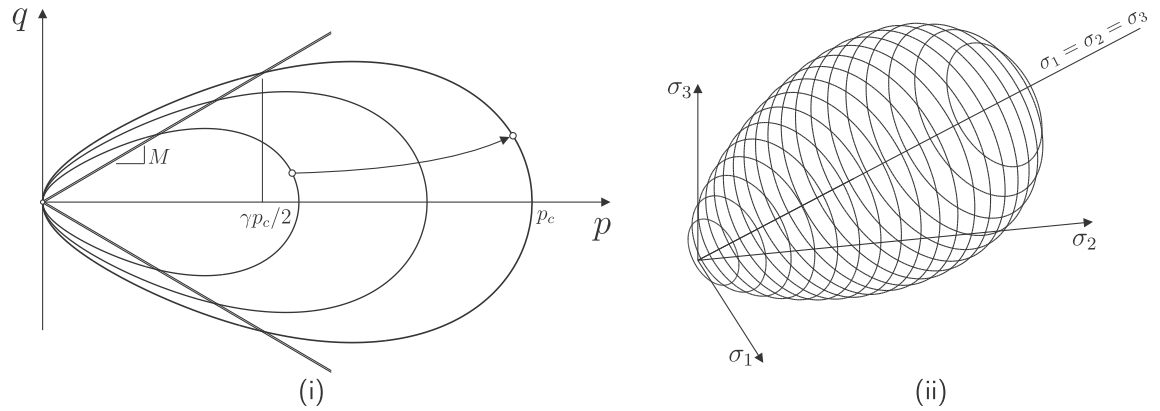

Fig. 3. Yield surfaces for $\alpha = 0.6$ and $\gamma = 0.9$ with no LAD (i) p–q stress space showing isotropic hardening (ii) principal stress space.

form of hardening implied by (19) and (20) gives rise to an isotropic expansion/contraction of the surface coupled with a (kinematic) translation along the hydrostatic axis, as shown in Fig. 3(i). We can now define the dissipative stress invariants as

$$p^{\varphi} = \frac{\partial \dot{\Phi}}{\partial \dot{\varepsilon}_v^{\mathrm{p}}} = \frac{A^2 \dot{\varepsilon}_v^{\mathrm{p}}}{\dot{\Phi}} \quad \text{and } q^{\varphi} = \frac{\partial \dot{\Phi}}{\partial \dot{\varepsilon}_\gamma^{\mathrm{p}}} = \frac{B^2 \dot{\varepsilon}_\gamma^{\mathrm{p}}}{\dot{\Phi}}. \tag{21}$$

Rearranging, we obtain the plastic strain rates as

$$\dot{\varepsilon}_v^{\mathrm{p}} = \frac{p^{\varphi}\dot{\Phi}}{A^2} \quad \text{and } \dot{\varepsilon}_\gamma^{\mathrm{p}} = \frac{q^{\varphi}\dot{\Phi}}{B^2}. \tag{22}$$

Substituting (22) into (16) and eliminating $\dot{\Phi}$, we obtain the dissipative yield condition

$$f^{\varphi} = (p^{\varphi})^2 B^2 + (q^{\varphi})^2 A^2 - A^2 B^2 = 0. \tag{23}$$

This defines an ellipse in dissipative $(p^{\varphi}, q^{\varphi})$ stress space. The dissipative stress invariants p^{φ} and q^{φ} are given by

$$p^{\varphi} = \frac{1}{3}\mathrm{tr}[\varphi] \quad \text{and } q^{\varphi} = \sqrt{\{s^{\varphi}\}^T\{s^{\varphi}\}}, \quad \text{where } \{s^{\varphi}\} = \{\varphi\} - p^{\varphi}\{1\}. \tag{24}$$

By substituting $(p\text{–}p^{\chi})$ for p^{φ} and q for q^{φ}, we arrive at the following expression for the yield function in true stress space

$$f = (p - \gamma p_c/2)^2 B^2 + q^2 A^2 - A^2 B^2 = 0. \tag{25}$$

For this f the Critical State Surface (CSS) takes the form of a Drucker–Prager circular cone. If $\alpha = \gamma = 1$, then $A = B = p_c/2$ and we recover the conventional modified Cam–Clay (MCC) yield function with associated plastic flow [37]. In this case, moving between dissipative and true stress space involves a constant hydrostatic translation of the yield surface, as A and B are only dependent on p_c. For values of $\gamma \in [0,1]$, the intersection of the CSS and the yield surface occurs at $p = \gamma p_c/2$. The value of α has no influence on that location. As γ reduces, the yield surface becomes narrower deviatorically (see Fig. 2(ii)). When $\gamma = 0$, the yield surface radius disappears. As α reduces, so the yield surface becomes more tear-drop shaped (with the tail at the stress origin); see Fig. 2. For $\alpha < 0.172$ the yield surface becomes concave near the stress origin (Fig. 2) [9]. When $\alpha = 0$ the yield surface lies entirely within the CSS.

Through the following simplification of (25), the yield function can be written as

$$\begin{aligned} f &= \left((p - \gamma p_c/2)^2 - A^2\right)B^2 + A^2 q^2, \\ &= \left(p^2 - \gamma p_c p + \gamma^2 (p_c)^2/4 - (1-\gamma)^2 p^2 - \gamma(1-\gamma)p_c p - \gamma^2 (p_c)^2/4\right)B^2 + A^2 q^2, \\ &= \left(\gamma(2-\gamma)p^2 - \gamma(2-\gamma)p_c p\right)B^2 + A^2 q^2, \\ &= \gamma p(2-\gamma)(p - p_c)B^2 + A^2 q^2 = 0. \end{aligned} \tag{26}$$

For this family of hyperplastic models, the direction of plastic flow is normal to the yield surface in *dissipative stress space*. Thus the dissipative plastic flow direction is formed by taking the derivative of (23) with respect to the dissipative stress

$$\{f^{\varphi}{}_{,\varphi}\} = (f^{\varphi}{}_{,p^{\varphi}})\{p^{\varphi}{}_{,\varphi}\} + (f^{\varphi}{}_{,q^{\varphi}})\{q^{\varphi}{}_{,\varphi}\}. \tag{27}$$

Using (24), (27) becomes

$$\{f^{\varphi}{}_{,\varphi}\} = \frac{2}{3}B^2 p^{\varphi}\{1\} + 2A^2\{s^{\varphi}\}. \tag{28}$$

Transforming into true stress space we obtain the direction of plastic flow as

$$\{g_{,\sigma}\} = \frac{2}{3}B^2(p - \gamma p_c/2)\{1\} + 2A^2\{s\}, \tag{29}$$

where the notation $\{g_{,\sigma}\}$ is used to suggest an equivalence with the derivative of the plastic potential used in conventional non-associated plasticity. Fig. 4 shows the direction of plastic flow for the two-parameter model with (i) $\alpha = 0.5$ and $\gamma = 1$ and (ii) $\alpha = 1$ and $\gamma = 0.5$.

Using (16) and $(19)_2$ we have obtained the yield surface, direction of plastic flow and the isotropic hardening equations, along with the hyperelastic relationship from (12), to fully define the constitutive relationship.

2.3. Lode angle dependency

The Lode angle is given by

$$\theta = \frac{1}{3}\arcsin\left(\frac{3\sqrt{3}}{2}\frac{J_3}{(J_2)^{3/2}}\right) \quad \in [-\pi/6, \pi/6], \tag{30}$$

where the invariants J_2 and J_3 are defined by $J_2 = (s_1^2 + s_2^2 + s_3^2)/2$ and $J_3 = (s_1^3 + s_2^3 + s_3^3)/3$, respectively. It has been shown that ignoring the dependence of constitutive relations on the third invariant of stress can lead to significant overestimation of the stiffness in geotechnical analyses [15,18,34]. A number of Lode angle dependencies have been proposed in the literature, for example [1,2,31,32,39,43]. Collins [9] combined the Matsuoka–Nakai yield condition with the Critical State cone by redefining q in the Spatially Mobilised Plane (SMP) [32]. However, implementing the Matsuoka–Nakai deviatoric yielding criteria in this manner constrains the principal admissible stress states to be compressive [8]. This can result in instabilities when constructing an implicit stress return algorithm where trial points lie in the tensile region.

Here we follow an alternative approach by introducing the LAD into the constitutive equations as follows

$$B_\theta = \bar{\rho}(\theta)B, \tag{31}$$

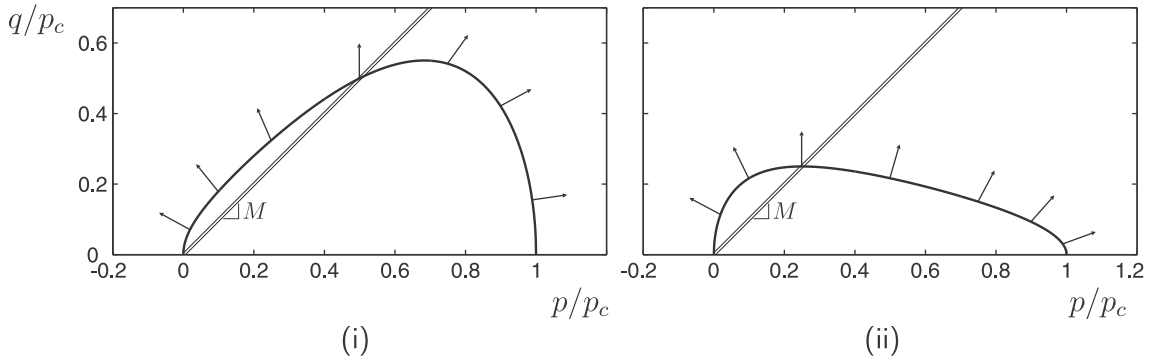

Fig. 4. Yield surfaces and direction of plastic flow for the two-parameter Critical State models: (i) $\alpha = 0.5$ and $\gamma = 1$ (ii) $\alpha = 1$ and $\gamma = 0.5$.

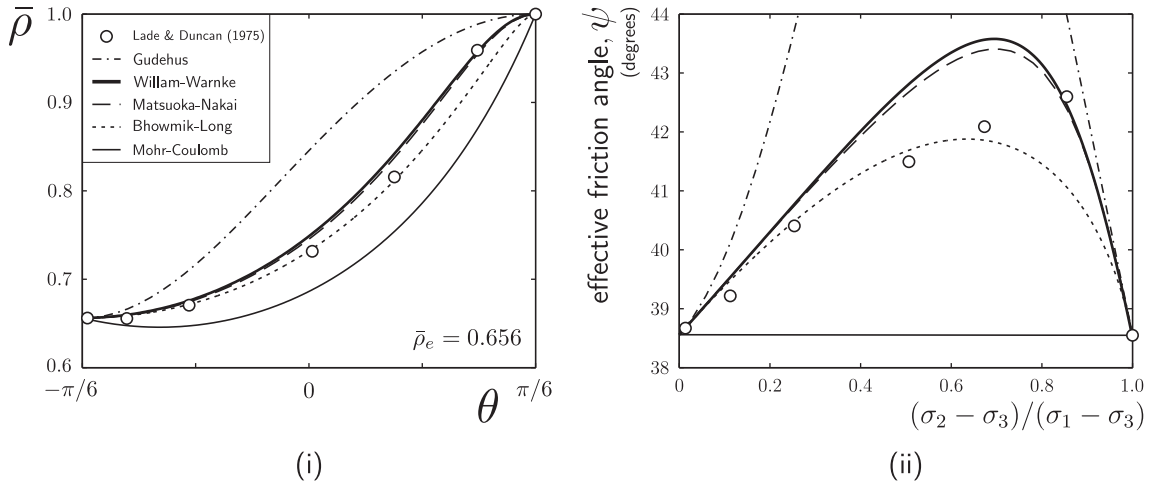

Fig. 5. Comparison of Lode angle deviatoric functions with experimental data from Lade and Duncan [31] (i) deviatoric function Lode angle dependency and (ii) variation of the effective friction angle with the ratio of the intermediate principal stress.

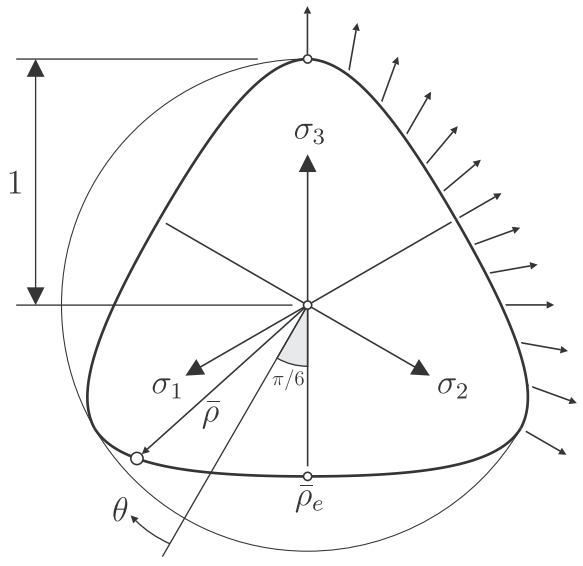

Fig. 6. Willam–Warnke deviatoric section illustrating the direction of the (non-associated) radial deviatoric plastic flow.

where B is given by (A.1)$_3$. $\bar{\rho}(\theta) = \rho(\theta)/\rho_c$ is the normalised deviatoric radius and ρ_c is the deviatoric radius required to reach yield under a triaxial compression stress path where $\sigma_3/2 = -\sigma_2 = -\sigma_1$. Fig. 5 compares Lode angle functions from [1,43,32,2] (with a normalised shear radius $\bar{\rho}_s = 0.73$ on the shear meridian) and [39] for $\bar{\rho}_e = 0.656$. $\bar{\rho}_e$ is the ratio of the deviatoric radius at yield under triaxial extension to the deviatoric radius (at the same mean stress) under triaxial compression. The multiaxial experimental data [31] shown in the figure indicate that geomaterials can have both a LAD (Fig. 5 (i)) and a sensitivity to the intermediate principal stress (Fig. 5(ii)). The effective friction angle in Fig. 5(ii) is calculated from the expression given by Griffiths [23]

$$\phi = \arcsin\left(\frac{\sqrt{3}\eta\cos(\theta)}{\sqrt{2} + \eta\sin(\theta)}\right), \tag{32}$$

where $\eta = q/(\sqrt{3}p)$. In Fig. 5, the M–C envelope (unlike the other deviatoric functions) exhibits no sensitivity to σ_2. The Gudehus LAD significantly overestimates both the normalised deviatoric radius and the effective friction angle. Although the Bhowmik–Long LAD arguably provides the most satisfactory fit to the experimental data, it requires an additional parameter $\bar{\rho}_s$ which can only be calibrated using a multiaxial test apparatus, of which there are very few. The W–W LAD provides a balance between offering good agreement with the experimental data yet requiring only one additional parameter, $\bar{\rho}_e$.

The W–W LAD (as seen in Fig. 6) can be expressed as

$$\bar{\rho}(\theta) = \frac{a_1 C + \sqrt{2a_1 C^2 + a_2}}{2a_1 C^2 + 1} \quad \in [\bar{\rho}_e, 1]$$
$$\text{where } a_1 = \frac{2(1-\bar{\rho}_e^2)}{(2\bar{\rho}_e - 1)^2}, \quad a_2 = \frac{5\bar{\rho}_e^2 - 4\bar{\rho}_e}{(2\bar{\rho}_e - 1)^2} \tag{33}$$

and $C = \cos(\theta + \pi/6)$. This describes a deviatoric section (with six-fold symmetry) formed by a portion of an ellipse. In the absence of triaxial extension data, we can estimate $\bar{\rho}_e$ based on the friction angle (ϕ) through

$$\bar{\rho}_e = \frac{2+k}{2k+1}, \quad \text{where } k = \frac{1+\sin(\phi)}{1-\sin(\phi)}, \tag{34}$$

so that $\bar{\rho}_e$ coincides with that of Mohr–Coulomb. The gradient M when $\theta = \pi/6$ is obtained (again from the friction angle) through the rearrangement of (32)

$$M = \frac{2\sqrt{6}\sin(\phi)}{3-\sin(\phi)}. \tag{35}$$

For other Lode angles, the gradient is given by $\bar{\rho}(\theta)M$. Note the non-standard definition of M based on the friction angle due to the definition of q from $(18)_1$, resulting in a difference of $\sqrt{2/3}$ between (35) and the standard definition. The yield equation and the direction of plastic flow are now expressed as

$$f = (\gamma p(2-\gamma)(p-p_c))(B_\theta)^2 + A^2q^2 = 0, \quad \text{and}$$
$$\{g_{,\sigma}\} = \frac{2}{3}(B_\theta)^2(p-\gamma p_c/2)\{1\} + 2A^2\{s\}. \tag{36}$$

The effect of introducing a W–W LAD on the different members of the family of constitutive models can be seen in Fig. 7. The three yield surfaces correspond to (i) $\alpha = \gamma = 1$, (ii) $\alpha = 0.5$, $\gamma = 1$ and (iii) $\alpha = 1$, $\gamma = 0.5$ with $\bar{\rho}_e = 0.8$ and a friction angle of $\phi = \pi/9$ radians.

2.4. Calibration of α and γ

The two material constants, α and γ, which extend the classical MCC model may be determined from examining undrained triaxial and one-dimensional consolidation data. In this calibration procedure we assume that, under sufficiently large straining during one-dimensional consolidation, the elastic strains are negligible. In this case the ratio of the deviatoric to volumetric plastic strains is

$$\frac{\dot{\varepsilon}^p_\gamma}{\dot{\varepsilon}^p_v} = \frac{A^2(\eta_{K_0})}{B^2(1-\gamma(p_c/p)/2)} = \sqrt{\frac{2}{3}}, \tag{37}$$

where $\eta_{K_0} = q/p$ is the stress ratio under one-dimensional (K_0) consolidation. Substituting (26) for B^2 and rearranging, we obtain the ratio of the size of the yield surface to the pressure as

$$\left(\frac{p_c}{p}\right) = \frac{\gamma(2-\gamma) + (\eta_{K_0})\sqrt{2/3}}{\gamma(2-\gamma) + \gamma(\eta_{K_0})\sqrt{1/6}}. \tag{38}$$

From (26), α can then be obtained as

$$\alpha = \frac{\left(\eta_{K_0}\right)(1+\gamma[(p_c/p)/2-1])(\gamma(2-\gamma)[(p_c/p)-1])^{-1/2} - M}{M(\gamma(p_c/p)/2-1)}. \tag{39}$$

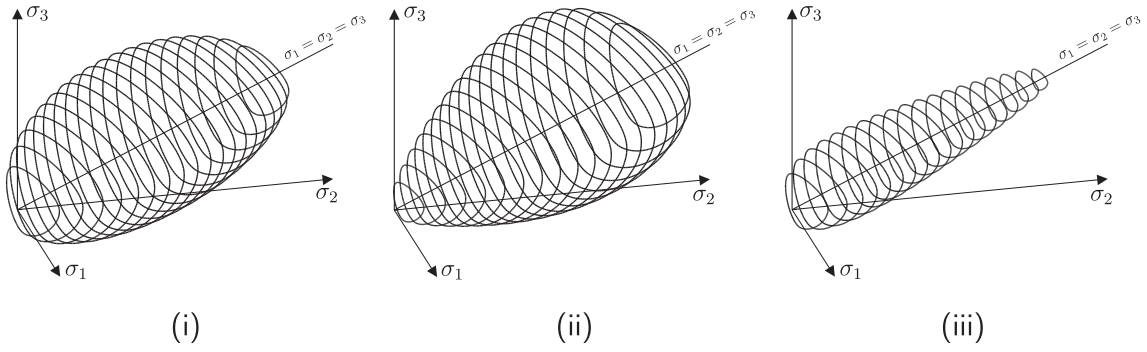

Fig. 7. Two-parameter Critical State family of models with W–W deviatoric sections: (i)$\alpha = \gamma = 1$, (ii) $\alpha = 0.5$, $\gamma = 1$ and (iii) $\alpha = 1$, $\gamma = 0.5$.

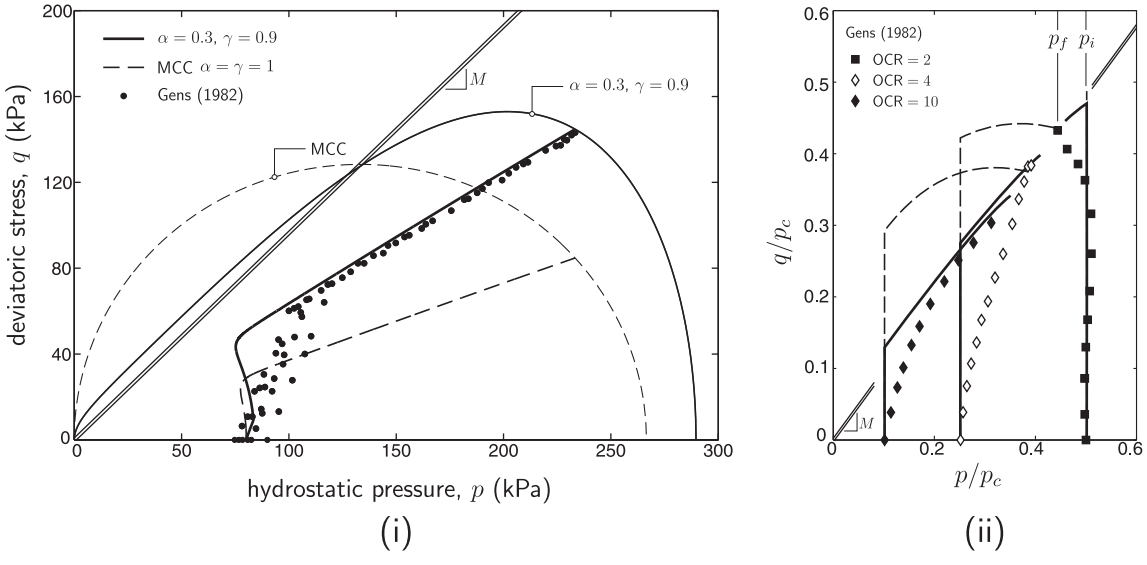

Fig. 8. Test simulations using the MCC model ($\alpha = \gamma = 1$) and the two-parameter model ($\alpha = 0.3$, $\gamma = 0.9$) compared against experimental data (shown by discrete points) from Gens [20]: (i) one-dimensional consolidation (ii) undrained triaxial compression with OCR = 2, 4 and 10 (the dashed line indicates the MCC model response, whereas the continuous line shows the stress path obtained from the two-parameter hyperplastic model).

However, (39) and (38) require the specification of γ which can be determined from undrained triaxial compression (UTC) or extension data at an overconsolidation ratio (OCR) of two. Fig. 8 (ii) shows UTC test results from Gens [20]. For OCR = 2, the change of normalised pressure between the starting and final stress states can be used to approximate γ, as shown in Fig. 8(ii), as

$$\gamma \approx \frac{p_f}{p_i} = \frac{2p_f}{p_c}, \tag{40}$$

where $p_i = p_c/2$ and p_f are the initial and final stress states from the UTC experiment. The change in the size of the yield surface will be small due to the near isochoric plastic flow (being in close proximity with the Critical State) such that $2p_f/p_c$ offers a reasonable approximation for γ.

In the absence of one-dimensional consolidation data, Jaky's [30] formula may be used to approximate the stress ratio under K_0 loading

$$\eta_{K_0} = \frac{\sqrt{6}\sin(\phi)}{3 - 2\sin(\phi)}, \tag{41}$$

where ϕ is the effective friction angle. Fig. 9(i) compares the experimental data collated by Federico et al. [19] with (41). Jaky's formula provides an adequate approximation to the experimental data, capturing the general trend. The value of α to achieve the K_0 consolidation stress ratio η_{K_0} for $\gamma = 0.8$, 0.9 and 1.0 is given in Fig. 9(ii) for both the experimental data collated by Federico et al. [19] and for Jaky's formula. For a friction angle of 25°, Jaky's formula predicts a stress ratio of $\eta_{K_0} = 0.480$ which is achievable with $\alpha = 0.336$, 0.246, 0.175 for $\gamma = 1.0$, 0.9 and 0.8, respectively.

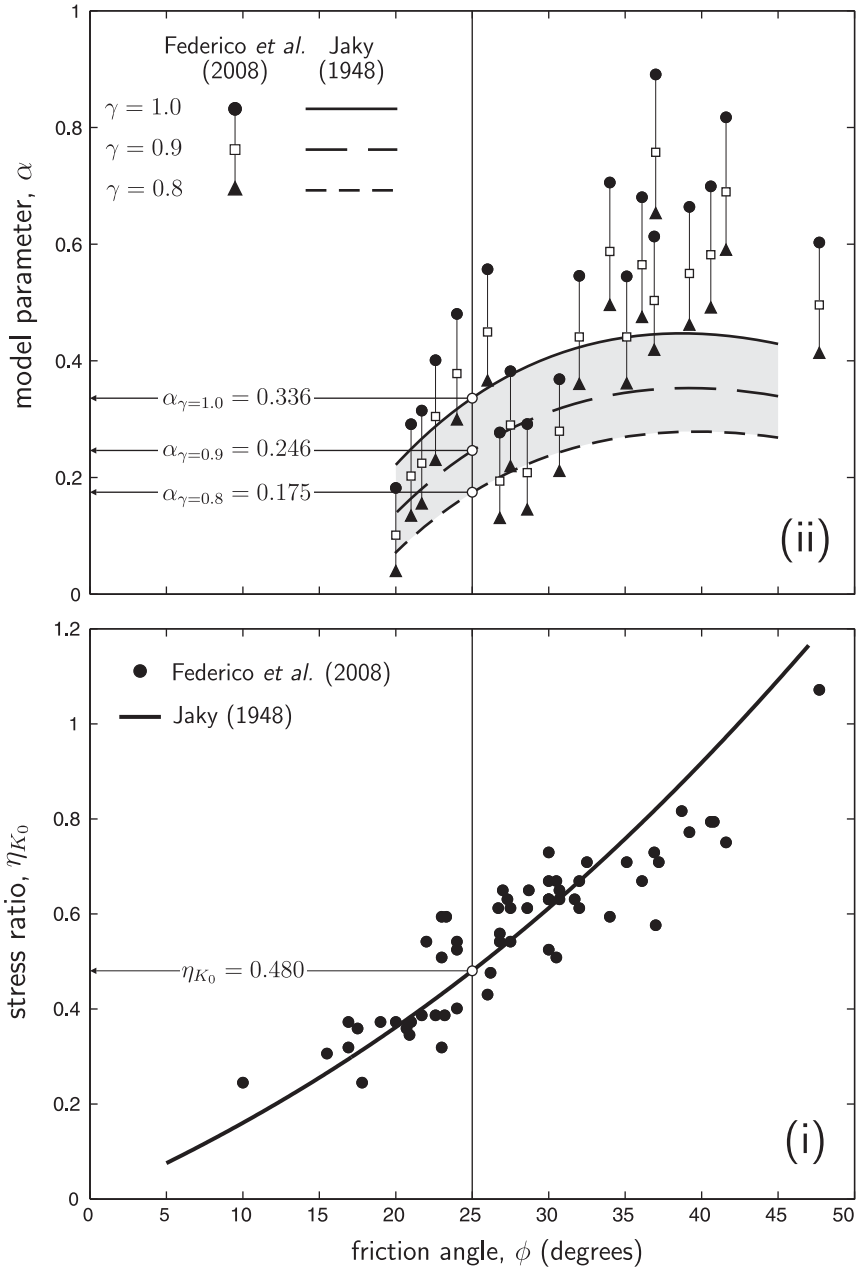

Fig. 9. Calibration of material constant α: (i) one-dimensional consolidation stress ratio against friction angle, comparing experimental data (discrete points) [19] against Jaky's equation [30] and (ii) α ranges for $\gamma = 0.8$, 0.9 and 1.0, corresponding to the data obtained from [19]. Graph (ii) also shows the α versus friciton angle relationships for $\gamma = 0.8$, 0.9 and 1.0 using Jaky's [30] relationship.

Fig. 8(i) compares the K_0 consolidation data on Lower Cromer Till (LCT) [20] with the MCC model and the two-parameter model. The experimental data achieves a stress ratio of $\eta_{K_0} = 0.6$, from Fig. 8(ii) $\gamma \approx 0.9$ and $M = 0.964$ ($\phi = 29.5°$). Using (38) and (39), we obtain $\alpha = 0.3$. The two-parameter model with $\alpha = 0.3$, $\gamma = 0.9$ provides an excellent fit to the K_0 experimental data. For the MCC model, once the gradient of the Critical State line has been specified, the stress path under one-dimensional consolidation is fixed (that is, K_0 is directly dependent upon M). In Fig. 8(i) we see that the MCC model is not able to provide a good simulation of the K_0 consolidation stress path. Fig. 8(ii) compares the UTC experimental data from Gens [20] with the response from the MCC model and the two-parameter model ($\alpha = 0.3, \gamma = 0.9$) for OCR = 2, 4 and 10. The two parameter model provides a significant improvement over the MCC formulation, as the latter significantly overpredicts the stress ratio $\eta = q/p$ prior to arrival at the Critical State.

3. Backward Euler stress integration

Stresses are integrated using the backward Euler scheme which corresponds to the minimisation of

$$\{\{\sigma_r\} - \{\sigma_t\}\}^T [C^e] \{\{\sigma_r\} - \{\sigma_t\}\}, \tag{42}$$

with respect to the return stress $\{\sigma_r\}$ (see Simo and Hughes [41]). This represents a closest point projection. Within (42), $(\cdot)_t$ and $(\cdot)_r$ denote quantities associated with the trial state and the return state respectively. The minimisation is subject to the following Karush–Kuhn–Tucker conditions

$$f \leqslant 0, \quad \dot{\gamma} \geqslant 0 \quad \text{and } f\dot{\gamma} = 0, \tag{43}$$

where $\dot{\gamma}$ is the plastic multiplier (not the deviatoric strain rate or the material parameter first seen in (16)). The popularity of the fully implicit BE approach over explicit schemes (for example [42]) is due to its relatively high accuracy for a given numerical effort, particularly when large strain increments are applied [5,41].

Working with elastic strains as the primary unknown, we can express the return mapping as

$$\{\varepsilon^e\} = \{\varepsilon_t^e\} - \Delta\gamma \{g_{,\sigma}\}, \tag{44}$$

where $\{\varepsilon_t^e\}$ is the elastic trial strain ($\{\varepsilon_t^e\} = \{\varepsilon_n^e\} + \{\Delta\varepsilon\}$; n refers to the converged state at the end of the previous increment and $\{\Delta\varepsilon\}$ is the current total strain increment), $\Delta\gamma$ is the incremental plastic multiplier for the entire return path and the plastic flow direction $\{g_{,\sigma}\}$ is determined at the final return state. The rate of the evolution of the size of the yield surface follows from $(19)_2$ as

$$\dot{p}_c = \left(\frac{\partial p_c}{\partial \varepsilon_v^p}\right) \dot{\varepsilon}_v^p = \left(\frac{p_c}{\lambda - \kappa}\right) \dot{\varepsilon}_v^p. \tag{45}$$

This hardening law is equivalent to specifying a bi-logarithmic linear relationship between specific volume and pre-consolidation pressure [3]. The limitations of the conventional linear relationship between specific volume (or void ratio) and the logarithm of the pre-consolidation pressure were identified by Butterfield [4]. More recently, the appropriateness of the bi-logarithmic law for finite deformation analysis was verified by Hashiguchi [25] and used by Yamakawa et al. [44]. Implicit integration of (45) yields the following hardening law

$$\tilde{p}_c = \frac{p_{c_n}}{(1 - \Delta\varepsilon_v^p/(\lambda - \kappa))}, \tag{46}$$

where p_{c_n} is the size of the yield surface from the previously converged solution associated with the last step (or the initial state at the start of the analysis). We denote the evolution of p_c with $\tilde{}$ to distinguish it from the incremental updating of p_c from the BE method through (61). Using (44) and (46) together with the consistency condition, $f = 0$, we can define the following residuals

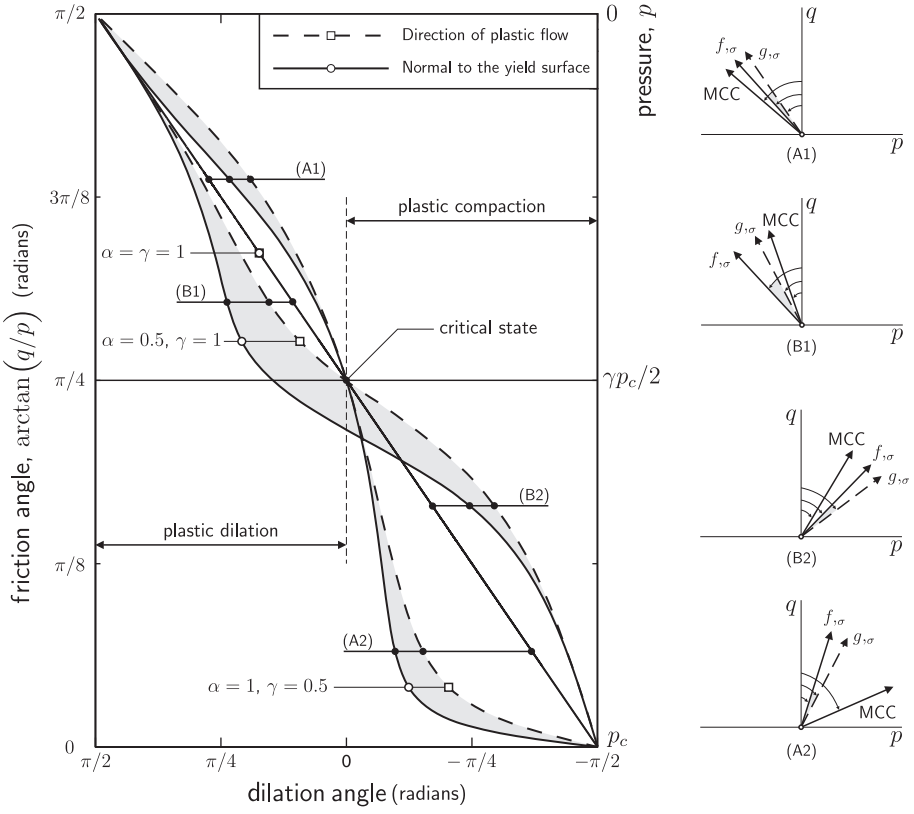

Fig. 10. Dilation angle for the plastic flow direction and the normal to the yield surface for $\alpha = \gamma = 1$, $\alpha = 0.5$, $\gamma = 1$ (B1–2) and $\alpha = 1$, $\gamma = 0.5$ (A1–2). The width of the shaded region indicates the degree of non-associatedness of the flow.

$$\{b\} = \begin{Bmatrix} \{b_1\} \\ b_2 \\ b_3 \end{Bmatrix} = \begin{Bmatrix} \{\varepsilon^e\} - \{\varepsilon_t^e\} + \Delta\gamma\{g_{,\sigma}\} \\ p_c - \tilde{p}_c \\ f \end{Bmatrix} = \begin{Bmatrix} \{0\} \\ 0 \\ 0 \end{Bmatrix}, \tag{47}$$

with unknowns

$$\{x\} = \{\{x_1\} \quad x_2 \quad x_3\}^T = \{\{\varepsilon^e\} \quad p_c \quad \Delta\gamma\}^T. \tag{48}$$

We obtain the (5×5) Jacobian matrix from the partial derivatives of the residuals with respect to the unknowns

$$[A] = \begin{bmatrix} [A_{11}] & \{A_{12}\} & \{A_{13}\} \\ \{A_{21}\}^T & A_{22} & A_{23} \\ \{A_{31}\}^T & A_{32} & A_{33} \end{bmatrix} = \begin{bmatrix} [b_{1,x_1}] & \{b_{1,x_2}\} & \{b_{1,x_3}\} \\ \{b_{2,x_1}\}^T & b_{2,x_2} & b_{2,x_3} \\ \{b_{3,x_1}\}^T & b_{3,x_2} & b_{3,x_3} \end{bmatrix}. \tag{49}$$

Forming this matrix, we obtain

$$[A] = \begin{bmatrix} [I] + \Delta\gamma[g_{,\sigma\sigma}][D^e] & \Delta\gamma\{g_{,\sigma p_c}\} & \{g_{,\sigma}\} \\ -\{\tilde{p}_{c,\sigma}\}^T[D^e] & 1 - (\tilde{p}_{c,p_c}) & -(\tilde{p}_{c,\Delta\gamma}) \\ \{f_{,\sigma}\}^T[D^e] & f_{,p_c} & 0 \end{bmatrix}, \tag{50}$$

where $[D^e]$ is the 3×3 elastic stiffness matrix (14). The derivatives of $\tilde{p}_c$ are given by

$$\{\tilde{p}_{c,\sigma}\}^T = \Delta\gamma p_n \{1\}^T [g_{,\sigma\sigma}],$$
$$(\tilde{p}_{c,p_c}) = \Delta\gamma p_n \{g_{,\sigma p_c}\}^T \{1\}, \quad (\tilde{p}_{c,\Delta\gamma}) = p_n \{g_{,\sigma}\}^T \{1\}, \tag{51}$$

with

$$p_n = \frac{\partial \tilde{p}_c}{\partial(\Delta\varepsilon_v^p)} = \frac{p_{c_n}}{(\lambda - \kappa)(1 - \Delta\varepsilon_v^p/(\lambda - \kappa))^2}. \tag{52}$$

The derivative of the yield function $(36)_1$ with respect to the principal stresses is given by

$$\{f_{,\sigma}\} = \frac{f_{,p}}{3}\{1\} + 2A^2\{s\} + 2\gamma\bar{\rho}(\theta)B^2 p(2-\gamma)(p - p_c)\{\bar{\rho}_{,\sigma}\}, \tag{53}$$

where

$$f_{,p} = (2-\gamma)\gamma(2\bar{\rho}(\theta)M(1-\alpha)(p - p_c)p + B_\theta(2p - p_c))B_\theta + 2A(1-\gamma)q^2. \tag{54}$$

The derivative $\{\bar{\rho}_{,\sigma}\}$ will depend on the implemented LAD. Taking the derivative of $(33)_1$ with respect to θ, we obtain

$$\bar{\rho}_{,\theta} = \frac{-a_1 S(b_1(1 + 2C/b_2) - 4C(a_1 C + b_2))}{b_1^2}, \quad \text{where}$$
$$b_1 = 2a_1 C^2 + 1, \quad b_2 = \left(2a_1 C^2 + a_2\right)^{1/2} \tag{55}$$

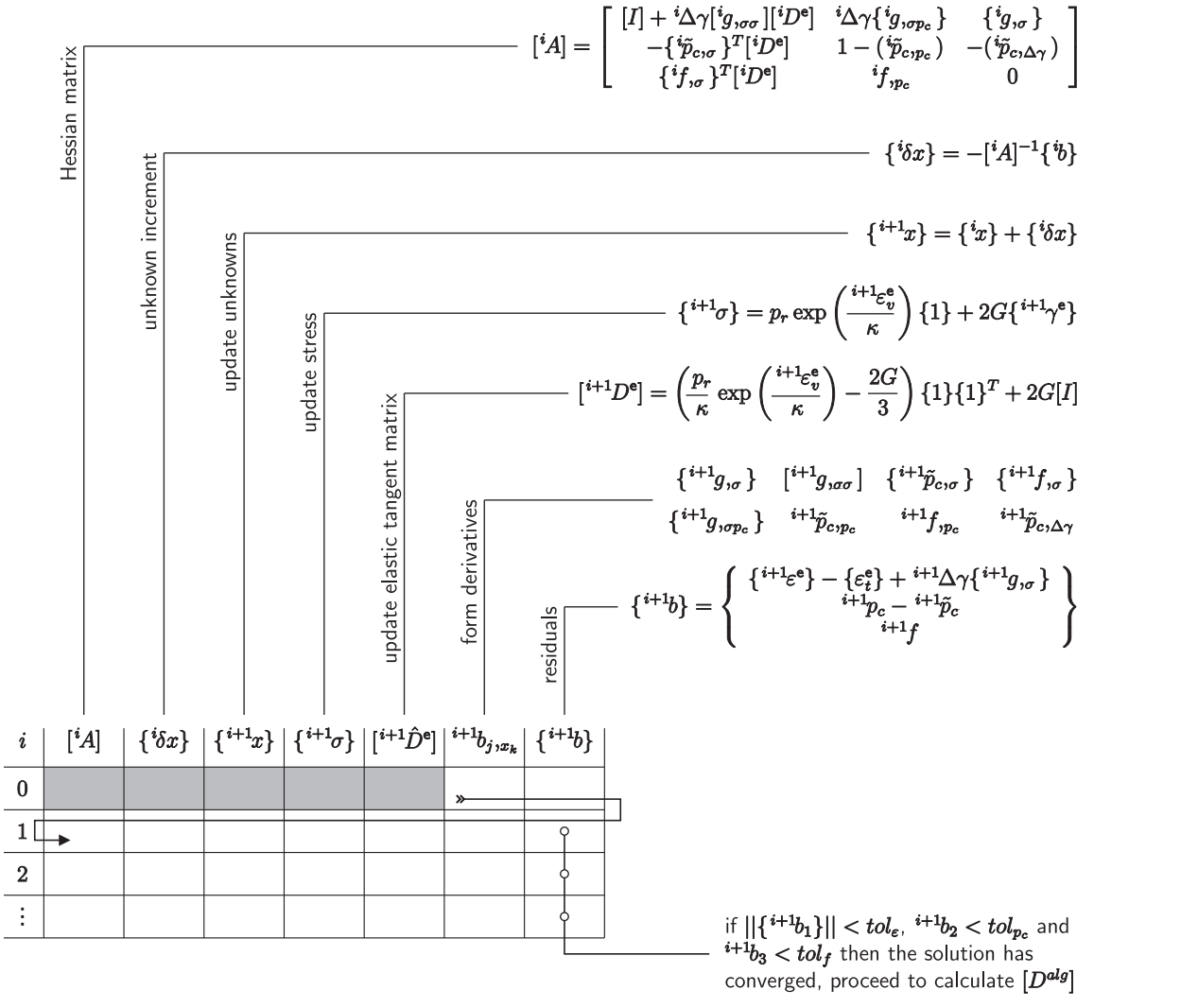

Fig. 11. Backward Euler stress return sequence.

and $S = \sin(\theta + \pi/6)$. The derivative of $\rho(\theta)$ with respect to $\{\sigma\}$ is obtained through the chain rule as

$$\bar{\rho}_{,\sigma} = \bar{\rho}_{,\theta}\{\theta_{,\sigma}\}, \tag{56}$$

where the derivative of the Lode angle with respect to stress is given in Appendix A.1.

Comparing (53) with $(36)_2$ it is apparent that incorporating a LAD within the constitutive model results in deviatorically non-associated plastic flow (Fig. 6). The model is also volumetrically non-associated (Fig. 4), except for the case $\alpha = \gamma = 1$, where the formulation reduces to the classical MCC (albeit with a W–W LAD). Fig. 10 illustrates the variation of the dilation angle $(-\arctan(\dot{\varepsilon}^p_v/\dot{\varepsilon}^p_\gamma))$ with the mobilised friction angle $(\arctan(q/p))$. It also shows the direction of the normal to the yield surface, for the case where $M = 1$. When $\alpha = 1$ the normals to the yield surface and the direction of plastic flow coincide at $q/p = M$ $(\arctan(q/p) = \pi/4)$, whereas for $\alpha \neq 1$ this is no longer the case. For $\alpha \neq 1$ and $\gamma \neq 1$ $\{f_{,\sigma}\}$ and $\{g_{,\sigma}\}$ only coincide at the stress origin and the compressive closure point on the hydrostatic axis (specifically at $p = 0$ and $p = p_c$). When $\alpha \neq 1$ or $\gamma \neq 1$, the normal to the plastic potential is oriented at a lower dilation angle than that given by the normal to the yield surface, for a given stress ratio q/p.

The derivative of $(36)_1$ with respect to p_c is given by

$$f_{,p_c} = \gamma\Big(p(2-\gamma)(\gamma\alpha\bar{\rho}(\theta)M(p-p_c) - B_\theta)B_\theta + Aq^2\Big). \tag{57}$$

From the direction of plastic flow $(36)_2$, the second derivative of the plastic potential with respect to $\{\sigma\}$ follows as

$$[g_{,\sigma\sigma}] = \frac{1}{3}\{g_{,\sigma p}\}\{1\}^T + 2A^2[\delta] + \frac{4}{3}\bar{\rho}(\theta)B^2(p - \gamma p_c/2)\{1\} \times \{\bar{\rho}_{,\sigma}\}^T, \tag{58}$$

where $[\delta] = [I] - \{1\}\{1\}^T/3$ and

$$\{g_{,\sigma p}\} = \frac{2}{3}\Big(B_\theta^2 + 2\bar{\rho}(\theta)MB_\theta(1-\alpha)(p - \gamma p_c/2)\Big)\{1\} + 4A(1-\gamma)\{s\}. \tag{59}$$

Finally, the derivative of $(36)_2$ with respect to p_c is obtained as

$$\{g_{,\sigma p_c}\} = \frac{\gamma B_\theta}{3}(2\alpha\bar{\rho}(\theta)M(p - \gamma p_c/2) - B_\theta)\{1\} + 2\gamma A\{s\}. \tag{60}$$

This provides the derivatives necessary to form (50).

Note that, as a consequence of the magnitude of f (with units of stress raised to the power four), it is necessary to divide f, $\{g_{,\sigma}\}$ and their associated derivatives by a large constant value when implementing the BE return to avoid the Hessian matrix becoming singular. Dividing by the trial yield function value offers a simple, effective remedy.

The iterative increment in the unknowns, $\{x\}$, is given by

$$\{\delta x\} = -[A]^{-1}\{b\}, \tag{61}$$

with the starting conditions

$$\{{}^0\varepsilon^e\} = \{\varepsilon^e_t\}, \quad {}^0\Delta\gamma = 0 \quad \text{and } {}^0p_c = p_{c_n}, \quad \therefore \quad \{{}^0b\} = \{\{0\} \quad 0 \quad {}^0f\}^T, \tag{62}$$

where the pre-superscript denotes the iteration number. The Newton–Raphson iterative process continues until the residuals converge to within a given tolerance. Throughout the stress return, all of the derivatives are evaluated at the current state. This requires the repeated evaluation of the derivatives at each iteration. The full sequence for the stress return is given in Fig. 11 where i indicates the current iteration number. The pseudo code for this algorithm is supplied in Fig. 12.

3.1. Stress return error analysis

The accuracy of the stress return algorithm was assessed over the range $1 \leqslant q_t/q_y \leqslant 10$ and $-\pi/6 \leqslant \theta \leqslant \pi/6$ for $p_t/p_{c_n} = 0.1$, 0.3, 0.5, 0.7 and 0.9 for three of the two-parameter models: $\alpha = \gamma = 1$ (MCC), $\alpha = \gamma = 0.5$ and $\alpha = 0.6$, $\gamma = 0.9$. q_y is the deviatoric yield stress under triaxial compression at a particular pressure p. A reference pressure of 100 kPa, compressibility index of $\kappa = 0.01$, initial elastic volumetric strain $\varepsilon^e_{v0} = 0$ and a shear modulus of $G = 2$ MPa

1. INPUT: $\{\varepsilon^e_t\}$, κ, λ, p_r, G, p_{c_n}, M, γ and α.
   (a) Transform the trial elastic strain $\{\varepsilon^e_t\}$ into principal strain components (that is, find the eigenvalues and associated eigenvectors)
   (b) Calculate the principal trial elastic stress $\{\sigma_t\}$ from (13)
   (c) Determine the trial yield function $(36)_1$
   (d) IF $f <$ `tol`
   - Elastic response, $\{\sigma\} = \{\sigma_t\}$ and $\{\varepsilon^e\} = \{\varepsilon^e_t\}$
   - $[D^{alg}] = [D^e]$ from (14)

   (e) ELSE
   - Elastoplastic response, set the initial conditions (62)
   - Calculate the derivatives required for (50)
   - WHILE $|\{b\}| >$ `tol` AND `itnum` $<$ `maxIt`
     - `itnum` $=$ `itnum` $+ 1$
     - Form the hessian matrix (50) and calculate the increment in the unknowns (61)
     - Calculate the updated unknowns $\{\varepsilon^e\}$, p_c and $\Delta\gamma$
     - Update $\{\sigma\}$ (13) and $[D^e]$ from $\{\varepsilon^e\}$ (14)
     - Calculate the derivatives required for (50)
     - Calculate the residuals $\{b\}$ (47)
   - Form the 6 component derivatives required for the consistent tangent from (70), and calculate the consistent tangent from (68).

   (f) Transform the principal measures back to generalised stress space using the eigenvectors from the trial elastic strain (A.7).
2. OUTPUT: $\{\varepsilon^e\}$, $\{\sigma\}$, $[D^{alg}]$ and p_c

Fig. 12. Pseudo code for the two-parameter family of Critical State models. The tolerance (`tol`) was typically set to 1×10^{-12}.

were used for the material's elastic properties. $p_{c_n} = 200$ kPa, $M = 0.6$, $\bar{\rho}^e = 0.8$ and $\lambda = 0.1$ define the yield surface. The starting point for the error analysis was a hydrostatic stress state equal to the pressure under consideration. The constitutive model then was subjected to a deviatoric elastic strain increment corresponding to the elastic trial stress state. The return stress from this single strain increment was compared with the solution obtained by splitting the strain increment into 1000 sub-increments.

The following error measure was used to assess the accuracy of the stress return algorithm

$$e = \frac{\sqrt{\{\{\sigma_r\} - \{\sigma_e\}\}^T \{\{\sigma_r\} - \{\sigma_e\}\}}}{\sqrt{\{\sigma_e\}^T \{\sigma_e\}}}, \tag{63}$$

where $\{\sigma_e\}$ is the *exact* stress return corresponding to the sub-incremented solution and $\{\sigma_r\}$ is the single increment BE return stress.

Stress iso-error maps are given in Fig. 13 for (i) $\alpha = \gamma = 1$ (MCC), (ii) $\alpha = \gamma = 0.5$ and (iii) $\alpha = 0.6$, $\gamma = 0.9$. Errors up to 28.0% appear for the $\alpha = \gamma = 0.5$ model at $p_t/p_{c_n} = 0.9$ when q_t/q_y is close to 10; this is not unexpected for such a large strain increment. For the same model at $p_t/p_{c_n} = 0.3$, the maximum error is less than 3.3%. All of the models have an error less than 5% for $q_t/q_y < 2$. For the majority of the pressure ratios (the exception being MCC for $p_t/p_{c_n} = 0.1$), higher errors (within a particular sextant), are seen near the compression meridians due to the higher curvature in the yield surface. The region of the lowest error, for all models, is near the *centre* of the yield surface ($p/p_c \simeq \gamma/2$) where there is lower meridional curvature in the surface and the direction of plastic flow is near isochoric. For $p_t/p_{c_n} = \gamma/2$ there is no error associated with the BE

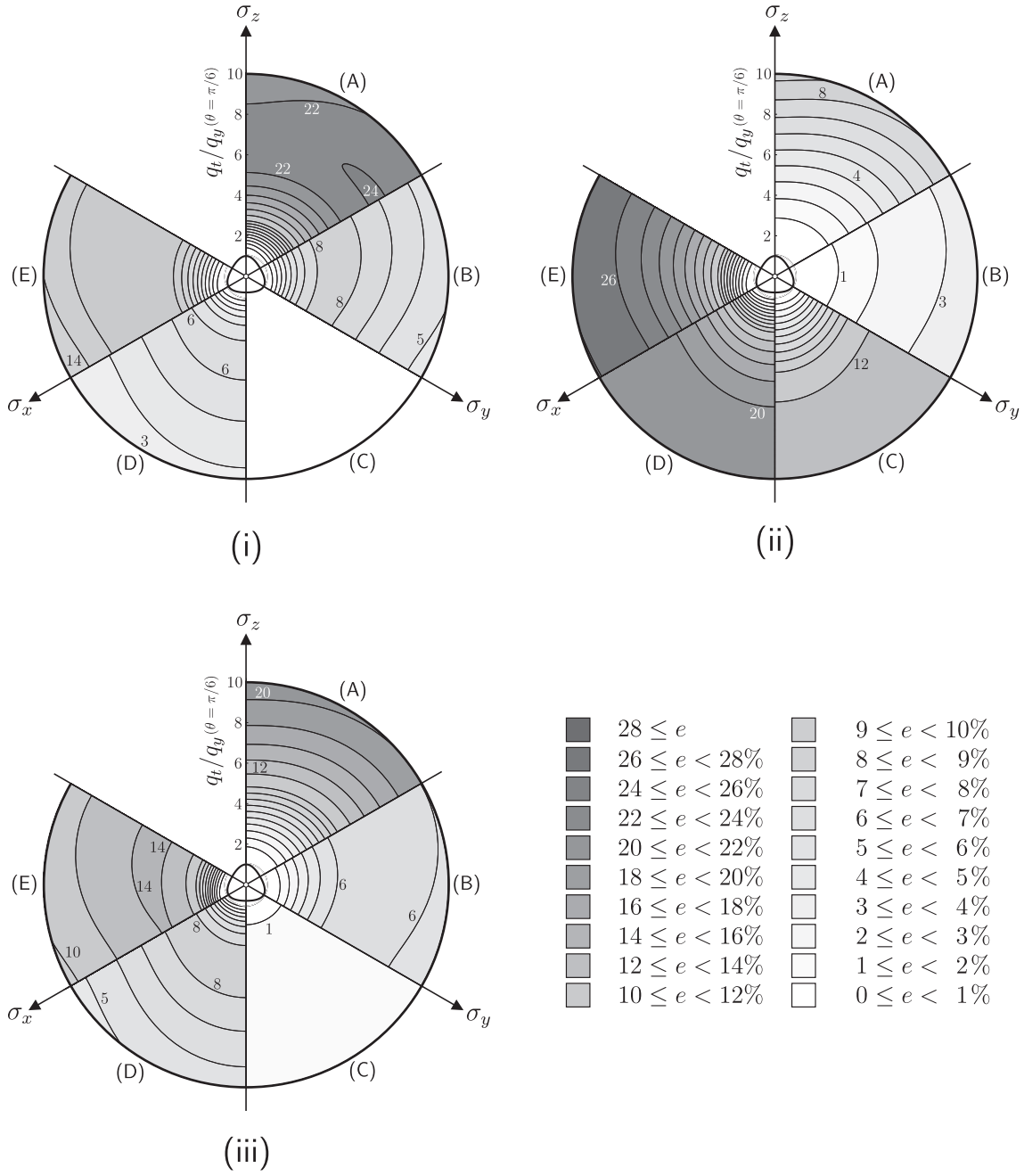

Fig. 13. Errors associated with the iterative BE stress return for five pressure ratios (A) $p/p_c = 0.1$, (B) $p/p_c = 0.3$, (C) $p/p_c = 0.5$, (D) $p/p_c = 0.7$ and (E) $p/p_c = 0.9$ for (i) $\alpha = \gamma = 1$, (ii) $\alpha = \gamma = 0.5$ and (iii) $\alpha = 0.6$, $\gamma = 0.9$.

Table 1
Error and return quantities associated with the iterative BE stress return for the five pressure ratios in Fig. 13 for $\alpha = \gamma = 1$, $\alpha = \gamma = 0.5$ and $\alpha = 0.6$, $\gamma = 0.9$.

	p_t/p_{c_n}	$\alpha = \gamma = 1$			$\alpha = \gamma = 0.5$			$\alpha = 0.6, \gamma = 0.9$		
		$\delta p_{c_{max}}/p_{c_n}$	it_{max}	e_{max}	$\delta p_{c_{max}}/p_{c_n}$	it_{max}	e_{max}	$\delta p_{c_{max}}/p_{c_n}$	it_{max}	e_{max}
(A)	0.1	−11.74%	7	24.08%	−4.48%	7	9.35%	−9.36%	7	20.889
(B)	0.3	−4.35%	8	8.46%	1.28%	8	3.25%	−3.29%	7	6.759
(C)	0.5	0.00%	8	0.00%	5.38%	8	13.65%	0.93%	8	1.909
(D)	0.7	3.09%	7	6.28%	8.18%	9	21.57%	4.05%	8	8.529
(E)	0.9	5.18%	7	11.62%	9.18%	8	28.02%	6.19%	8	14.239

return, as shown by Fig. 13(i) sextant (C). In this case the trial stress will return radially onto the original yield surface at the intersection with the Critical State following isochoric plastic flow. The highest errors are in regions of high curvature and high volumetric plastic flow. The maximum error (e_{max}), maximum number of iterations required to find convergence (it_{max}) and the largest change in the size of the yield surface ($\Delta p_{c_{max}}$) are given in Table 1 for all three of the models under consideration. For the MCC model, the maximum error of 24.1% occurs at $p_t/p_{c_n} = 0.1$. In the lower pressure ratios, the yield surface of the MCC model softens more than the other models. The opposite is seen for the high pressure ratios, with greatest errors and the largest hardening of the yield surface associated with the $\alpha = \gamma = 0.5$ model. Fig. 13 and Table 1 confirm the well-behaved nature of the integration scheme for the two-parameter family of Critical State models.

4. Consistent tangent

The use of the consistent tangent within the global Newton–Raphson (N–R) iterations allows for asymptotic quadratic convergence for the residual out-of-balance force [40]. In this section we present the consistent tangent for the family of hyperplastic models with a W–W LAD deviatoric section. That tangent is defined as

$$[D^{alg}] = \left[\sigma_{,\varepsilon_t^e}\right]. \tag{64}$$

It is obtained through minimising the residuals (47) with respect to the trial elastic strain, $\{\varepsilon_t^e\}$. The first row of (47) becomes

$$[\widehat{C}^e]\{d\hat{\sigma}\} + \Delta\gamma\left([\hat{g}_{,\sigma\sigma}]\{d\hat{\sigma}\} + \{\hat{g}_{,\sigma p_c}\}d\hat{p}_c\right) + d\Delta\gamma\{\hat{g}_{,\sigma}\} = \{d\hat{\varepsilon}_t^e\}, \tag{65}$$

where $(\hat{\cdot})$ denotes six component vectors and matrices. Considering the second row, we obtain

$$dp_c - (\tilde{p}_{c,p_c})dp_c - \{\hat{\tilde{p}}_{c,\sigma}\}^T\{d\hat{\sigma}\} - (\tilde{p}_{c,\Delta\gamma})d\Delta\gamma = 0. \tag{66}$$

Finally the third row, from the consistency condition, yields

$$\{\hat{f}_{,\sigma}\}^T\{d\hat{\sigma}\} + f_{,p_c}dp_c = 0. \tag{67}$$

Combining (65)–(67), we have

$$\underbrace{\begin{bmatrix} [\widehat{C}^e] + \Delta\gamma[\hat{g}_{,\sigma\sigma}] & \Delta\gamma\{\hat{g}_{,\sigma p_c}\} & \{\hat{g}_{,\sigma}\} \\ -\{\hat{\tilde{p}}_{c,\sigma}\}^T & 1 - (\tilde{p}_{c,p_c}) & -(\tilde{p}_{c,\Delta\gamma}) \\ \{\hat{f}_{,\sigma}\}^T & f_{,p_c} & 0 \end{bmatrix}}_{[A^{alg}]^{-1}} \begin{Bmatrix} \{d\hat{\sigma}\} \\ dp_c \\ d\Delta\gamma \end{Bmatrix} = \begin{Bmatrix} \{d\hat{\varepsilon}_t^e\} \\ 0 \\ 0 \end{Bmatrix}. \tag{68}$$

Multiplying both sides of (68) by $[A^{alg}]$, we obtain

$$\begin{Bmatrix} \{d\hat{\sigma}\} \\ dp_c \\ d\Delta\gamma \end{Bmatrix} = \begin{bmatrix} [\widehat{D}^{alg}] & \{A_{12}^{alg}\} & A_{13}^{alg} \\ \{A_{21}^{alg}\}^T & A_{22}^{alg} & A_{23}^{alg} \\ \{A_{31}^{alg}\}^T & A_{32}^{alg} & A_{33}^{alg} \end{bmatrix} \begin{Bmatrix} \{d\hat{\varepsilon}_t^e\} \\ 0 \\ 0 \end{Bmatrix}, \tag{69}$$

where $[\widehat{D}^{alg}]$ is the six-component algorithmic consistent tangent. The six-component vectors and matrices required in (68) are given by

$$\{\hat{\cdot}\} = \begin{Bmatrix} \{\cdot\} \\ \{0\} \end{Bmatrix} \quad \text{and} \quad [\hat{g}_{,\sigma\sigma}] = \begin{bmatrix} [g_{,\sigma\sigma}] & [0] \\ [0] & 2A^2[I] \end{bmatrix}. \tag{70}$$

The consistent tangent from (69) must be transformed (through (A.7)) using the eigenvectors associated with the trial elastic strain to obtain a stiffness matrix consistent with the six component stresses and strains.

5. Numerical analysis

5.1. Material point analysis

In this section we make comparisons with experimental data using two examples from the two-parameter family of Critical

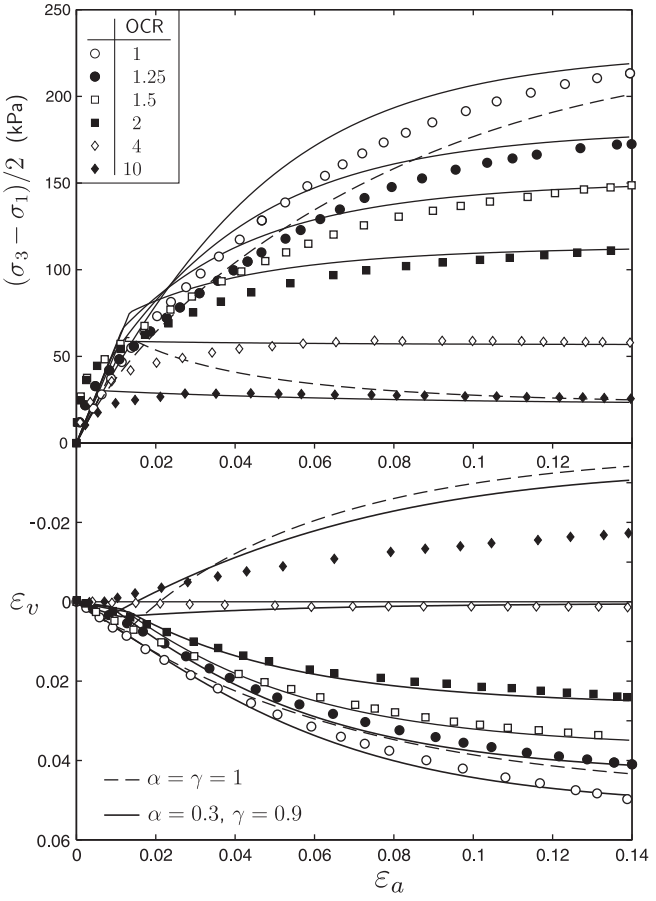

Fig. 14. Drained triaxial compression test simulations compared with experimental data (shown by discrete points) [20]. Above: axial strain (ε_a) against deviatoric stress ($(\sigma_3 - \sigma_1)/2$). Below: axial strain (ε_a) against volumetric strain (ε_v).

State hyperplastic models. A reference pressure of 100 kPa, compressibility index of $\kappa = 0.0073$, initial elastic volumetric strain $\varepsilon^e_{v0} = 0$ and a shear modulus of $G = 4$ MPa were used for the material's elastic properties. $p_c = 233.3$ kPa, $M = 0.964$, $\lambda = 0.0447$ and $\bar{\rho}_e = 0.729$ define the yield surface, as obtained by Dafalias et al. [17] (note that Dafalias used a linear relationship between void ratio and the logarithm of effective pressure rather than the bi-logarithmic relationship adopted in this paper, resulting in different values for κ and λ).

Fig. 14 illustrates the material responses given $\alpha = \gamma = 1$ (MCC) and $\alpha = 0.3$, $\gamma = 0.9$ under drained triaxial compression for six over-consolidation ratios (OCR = 1, 1.25, 1.5, 2, 4 and 10). The results are compared against experimental data from Gens [20]. In these tests, the material was initially under a hydrostatic stress state with $p = 233.3$, 186.7, 155.6, 166.7, 58.3 and 23.3 kPa, corresponding to the six OCRs. The material was subsequently compressed axially whilst maintaining a constant lateral pressure. The two-parameter model with $\alpha = 0.3$, $\gamma = 0.9$ provides an improved fit over the MCC model to the experimental data (for all OCRs) in terms of $(\sigma_3 - \sigma_1)/2$. These results illustrate the benefits of the yield surface having a form where the envelope is contracted towards the Critical State line when $q/p > M$ (recall Fig. 3).

Fig. 15 shows the drained triaxial compression stress paths for four OCRs together with the cumulative plastic work and energy dissipation for the same two-parameter model. For overconsolidation ratios less than $2/\gamma$, hardening takes place and the plastic work is greater than the dissipated energy. Whereas for overconsolidation ratios greater than $2/\gamma$, softening occurs and the converse is true. The rate of plastic work and plastic dissipation are given by (11) and (7), respectively, where $\chi_{ij} = (\gamma p_c/2)\delta_{ij}$ and $\varphi_{ij} = \sigma_{ij} - \chi_{ij}$. When the hydrostatic pressure, p, drops below $\gamma p_c/2$, the product of the shift stress with the plastic strain rate becomes negative (due to the dilative plastic strains) resulting in the total plastic work being less than the dissipation.

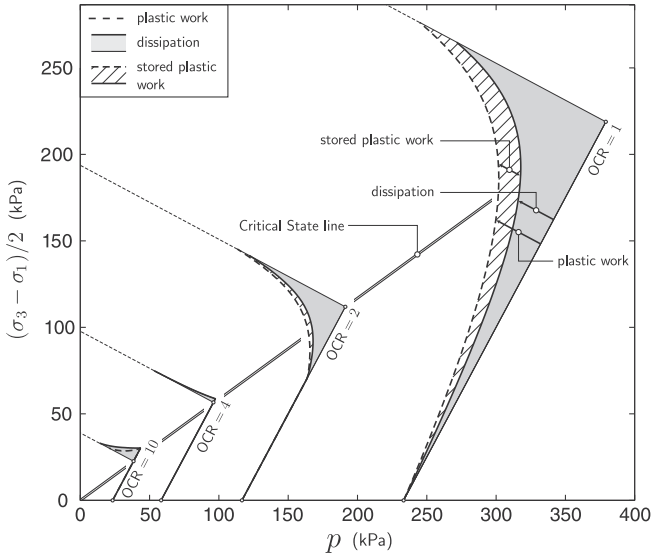

Fig. 15. Drained triaxial compression stress paths showing the cumulative plastic work and dissipation for the two-parameter model with $\alpha = 0.3$ and $\gamma = 0.9$.

5.2. Strain probing

The concepts of stored plastic work and dissipation are illustrated further in Fig. 16 which presents Gudehus plots [24] for $\alpha = 0.6$ and $\gamma = 0.9$. A reference pressure of 100 kPa, compressibility index of $\kappa = 0.0073$, initial elastic volumetric strain $\varepsilon^e_{v0} = 0$ and a shear modulus of $G = 4$ MPa were used for the material's elastic properties. $p_c = 233.3$ kPa, $M = 0.964$, $\lambda = 0.0447$ and $\bar{\rho}_e = 0.729$ define the yield surface.

The model is subjected to 832 strain probes for 64 *spheres* starting at different locations on the yield surface. Each *sphere* has a strain radius of 1000μ (that is, 1×10^{-3}). The directions of the individual strain probes are obtained using the HEALPix software [22], dividing the surface of the sphere into equal area patches. Figs. 16(i) and (ii) show the stress response (known as Gudehus plots [24]) to these strain spheres. The Gudehus surfaces are shaded according to the degree of (i) dissipated and (ii) stored plastic work. The maximum and minimum work for each stress surface are scaled to 1 and 0. These correspond to 164.6 J/m^3 and -68.8 J/m^3, respectively.

Fig. 17 presents a sequence of Gudehus plots for the model with the same material parameters as above but with $p_c = 300$ kPa. Fig. 17(i) shows results in the σ_x–σ_y plane. Fig. 17(ii) gives the same plots viewed in the deviatoric plane. The model starts at a randomly selected point on the yield surface and is subjected to

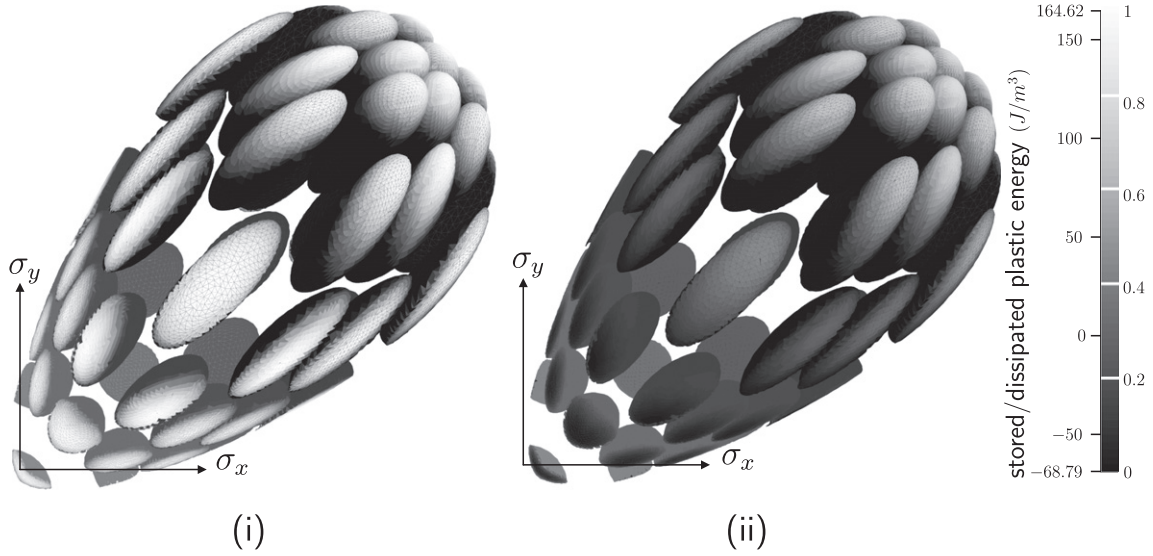

Fig. 16. Three dimensional Gudehus stress plots with shading according to (i) dissipated plastic energy and (ii) stored plastic energy. The maximum and minimum work for each stress surface is identified by 1 and 0 corresponding to 164.6 J/m^3 and -68.8 J/m^3, respectively.

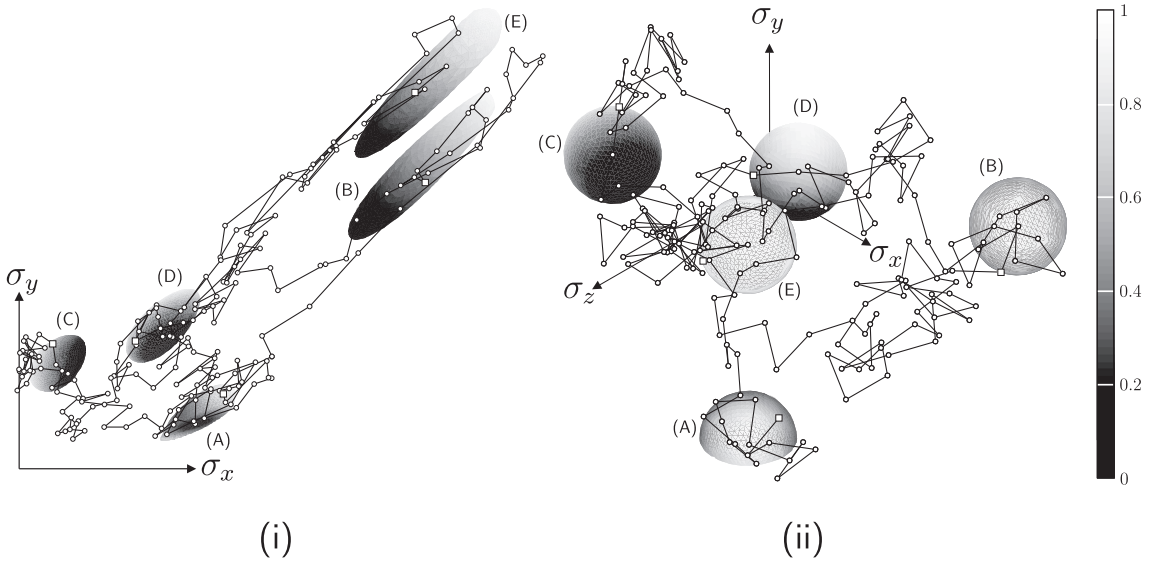

Fig. 17. Sequence of Gudehus stress plots demonstrating the robustness of the BE stress return algorithm for (i) σ_x–σ_y plane and (ii) deviatoric view. The surfaces are shaded according to the length of the stress path with the maximum and minimum length identified by 1 and 0, respectively. Five of the 200 Gudehus plots are presented for steps 1 (A), 50 (B), 100 (C), 150 (D) and 200 (E).

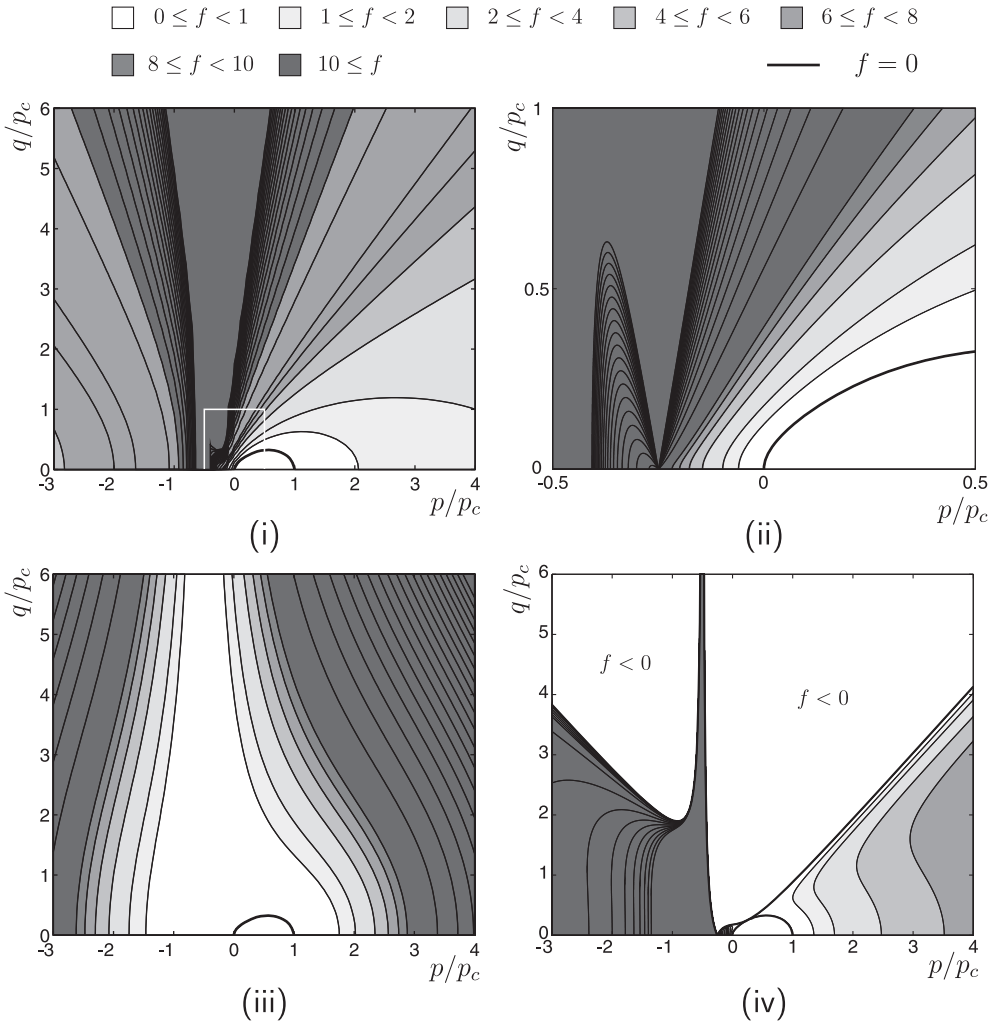

Fig. 18. Contours of the yield function outside of the yield surface for a two-parameter Critical State model where $\alpha = \gamma = 0.5$ (i) f given by (71) from [7,11,8,9], (ii) local detail of f given by (71), (iii) f given by $(36)_1$ and (iv) f from (73) with negative regions appearing outside the yield surface.

1,280 strain probes in directions determined by HEALPix. Once again, the probes are each of length $\sqrt{\{\Delta\varepsilon\}^T\{\Delta\varepsilon\}} = 10^{-3}$. The stress responses and internal material parameters are stored before advancing to the next Gudehus plot. One of the probe responses is randomly chosen as the starting point for the next strain sphere. Five of the 200 stress responses are plotted for probes 1, 50, 100, 150 and 200, where the surfaces are shaded according to the distance from the starting stress state to the return stress state. The stress path between the starting points for the strain spheres is also plotted. As the pressure increases so does the elongation of the stress response. This is due to the pressure-sensitive nonlinear elasticity providing an increase in stiffness with pressure. The stress responses, when inside the yield surface, have a circular deviatoric section due to the elastic isotropy. The Gudehus plots are flattened in the direction of the yield surface as most of the strain increment is taken up by the plastic response, leaving little for the elastic (and hence stress) response. The smoothness of the stress return surfaces shown in Fig. 17 serves to demonstrate the well behaved nature and robustness of the implemented constitutive model.

5.3. Influence of f

The form of the yield function, f, significantly affects the robustness and efficiency of the BE stress integration method. The function given by $(36)_1$ (with $\bar{\rho}^e = 1$) is quite different to that used by Collins et al. [7–9,11] who adopted the form

$$f = \frac{(p - \gamma p_c/2)^2}{A^2} + \frac{q^2}{B^2} - 1 = 0. \tag{71}$$

Manipulating (23) we can obtain any number of different forms of the yield function in dissipative stress space. Through one such manipulation, we can obtain the yield function in dissipative stress space as

$$f^{\varphi} = \frac{(p^{\varphi})^4}{A^4} - \left(1 - \frac{(q^{\varphi})^2}{B^2}\right)^2 = 0, \tag{72}$$

which transforms to become

$$f = \frac{(p - \gamma p_c/2)^4}{A^4} - \left(1 - \frac{q^2}{B^2}\right)^2 = 0 \tag{73}$$

in true stress space. (26), (71) and (73) describe the same yield surface. However, the nature of the yield function outside of the yield surface ($f > 0$) is very different for the three cases. Fig. 18 shows contours of f outside the yield surface for (i) (71), (iii) $(36)_1$ and (iv) (73) when $\alpha = \gamma = 0.5$ and $\bar{\rho}_e = 1$. Note that these plots have been made for the case where no LAD is present. Thus the deviatoric stress return is radial in this illustrative example. When $10 < f < 200$, the contours are plotted in intervals of 10. For (71), Fig. 18(i), we see a local minimum around $(p/p_c) = -3$ and very high local curvature plus a maximum around $(p/p_c) = -0.5$ (see detail in Fig. 18(ii)). The presence of these minima and maxima could cause significant problems for a BE stress return algorithm. These difficulties are completely removed by using $(36)_1$; see Fig. 18(iii). (73) contains negative regions outside the yield surface, as shown in Fig. 18(iv). If a trial stress state is located within one of these regions then the constitutive model falsely predicts a purely elastic response despite the stress being outside the yield surface.

Fig. 19 shows stress returns for the three forms of f: $(36)_1$, (71) and (73). A reference pressure of 100 kPa, compressibility index of

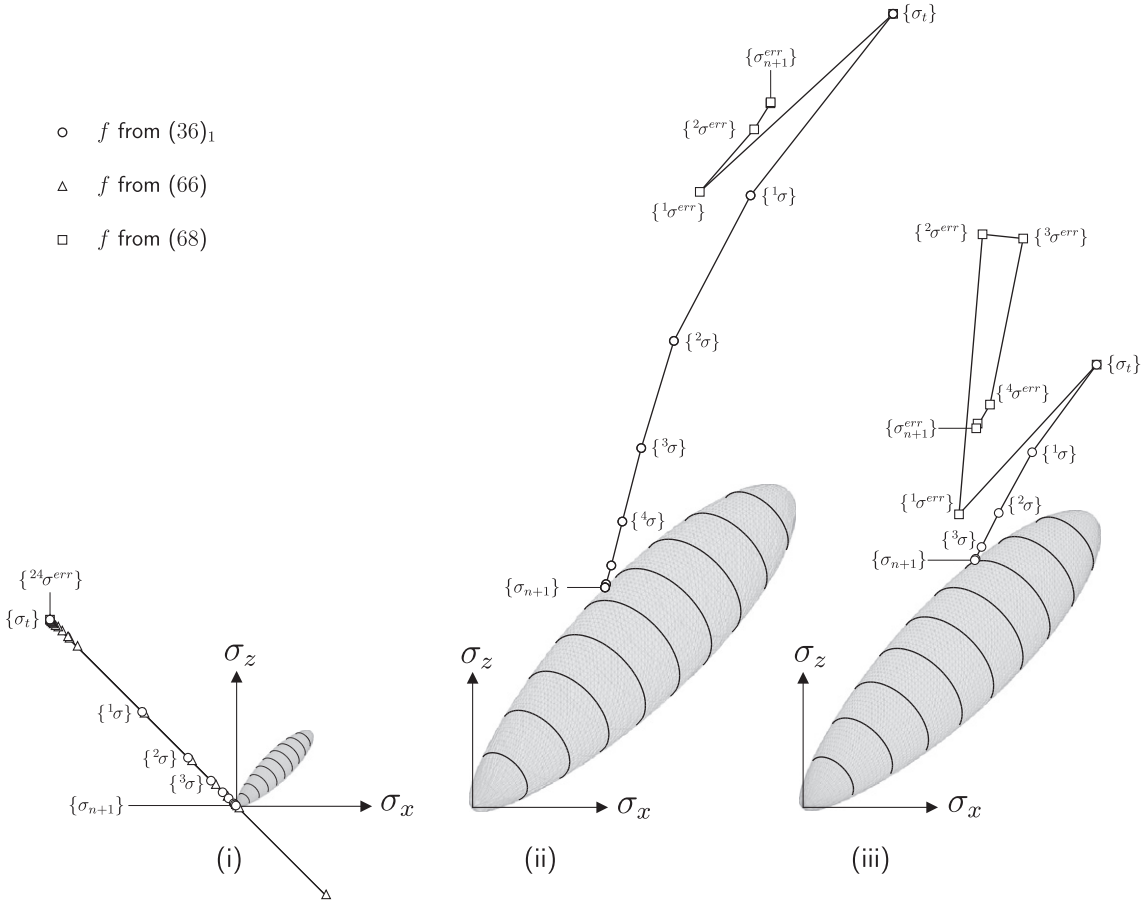

Fig. 19. Stress returns (associated with yield functions $(36)_1$, (71) and (73)) for three different trial states (i)–(iii).

$\kappa = 0.01$, initial elastic volumetric strain $\varepsilon^{e}_{v0} = 0$ and a shear modulus of $G = 2$ MPa were used for the material's elastic properties. $p_c = 200$ kPa, $M = 0.6$, $\lambda = 0.1$, $\alpha = 0.5$, $\gamma = 0.5$ and $\bar{\rho}_e = 1$ define the yield surface. The models are subjected to a trial elastic strain state, as given in Table 2, and their return paths observed. The size of the yield surface displayed in Fig. 19 corresponds to the final $p_{c_{n+1}}$ value from the stress return associated with $(36)_1$.

In Fig. 19(i) the different returns associated with the three forms of the yield function are compared. The trial state has zero pressure. This provides a particularly challenging state from which to start a BE stress integration. The values of the trial yield function (f_t), trial stress state ($\{\sigma_t\}$), final stress state ($\{\sigma_{n+1}\}$), final size of the yield surface ($p_{c_{n+1}}$) and the number of iterations to find convergence are given in Table 2. The value of the yield function (73) at the trial state is negative, thus the constitutive model predicts an elastic response, which is clearly incorrect for that trial stress. (71) fails to converge after 24 iterations and the size of the yield surface takes a meaningless negative value. The stress state after the 24th iteration is denoted by $\{^{24}\sigma^{err}\}$. The return path oscillates either side of the stress origin, unable to converge to back onto the yield surface. Only the model with the yield function described by $(36)_1$ converges to the appropriate stress state, although 19 iterations are required to converge within the specified tolerance. In this case the yield surface has contracted (softened) to 27% of its original size due to the significant plastic dilation associated with the stress return.

Fig. 19(ii) and (iii) demonstrate stress returns for the yield functions described by $(36)_1$ and (73). For both trial states, (73) converges to a stress ($\{\sigma^{err}_{n+1}\}$) associated with $f = 0$ outside the yield surface, rather than onto the correct yield surface. These false stress returns produce an inappropriate $p_{c_{n+1}}$ value and give rise to the incorrect consistent tangent matrix. $(36)_1$ correctly converges back onto the yield surface for both trial stress states in eight and six iterations (Fig. 19(ii) and (iii)), respectively.

The stress returns shown in Fig. 19 demonstrate the importance of using an appropriate form of f for the BE integration scheme, and confirm that $(36)_1$ provides a more robust expression than (71) (or (73)).

5.4. Single element test

A simple small strain finite element analysis was first undertaken to assess the constitutive model's performance within a general purpose 3D code. A single unit-cube (8-noded hexahedral element) constrained on its lower horizontal and two vertical faces was initially subjected to a uniform hydrostatic pressure of

Table 2
Stress return values for different yield functions (see Fig. 19).

	f	f_t	$\{\epsilon^e_t\}$	σ_t (kPa)	$\{\sigma_{n+1}\}$ (kPa)	$p_{c_{n+1}}$ (kPa)	Iterations
(i)	$(36)_1$	9.492×10^{19} pa^4			$\{-0.156 \quad 0.0016 \quad 0.189\}^T$	54.09	19
	(71)	1.688×10^2	$\begin{Bmatrix} -0.1444 \\ -0.1100 \\ -0.0756 \end{Bmatrix}$	$\begin{Bmatrix} -137.78 \\ 0 \\ 137.78 \end{Bmatrix}$	$\{-137.54 \quad 0 \quad 137.54\}^T$	-6.787×10^6	24 +
	(73)	-2.814×10^4			$\{-137.78 \quad 0 \quad 137.78\}^T$	200	0
(ii)	$(36)_1$	4.715×10^{21} pa^4	$\begin{Bmatrix} -0.0294 \\ 0.0050 \\ 0.0394 \end{Bmatrix}$	$\begin{Bmatrix} 310.39 \\ 448.17 \\ 585.95 \end{Bmatrix}$	$\{97.75 \quad 130.06 \quad 162.38\}^T$	231.87	8
	(73)	3.9639			$\{220.09 \quad 370.40 \quad 520.72\}^T$	204.33	5
(iii)	$(36)_1$	3.465×10^{20} pa^4	$\begin{Bmatrix} 0.0104 \\ 0.0330 \\ 0.0171 \end{Bmatrix}$	$\begin{Bmatrix} 216.71 \\ 271.83 \\ 326.94 \end{Bmatrix}$	$\{126.74 \quad 154.62 \quad 182.49\}^T$	213.38	6
	(73)	1.905			$\{128.82 \quad 206.09 \quad 283.37\}^T$	206.35	7

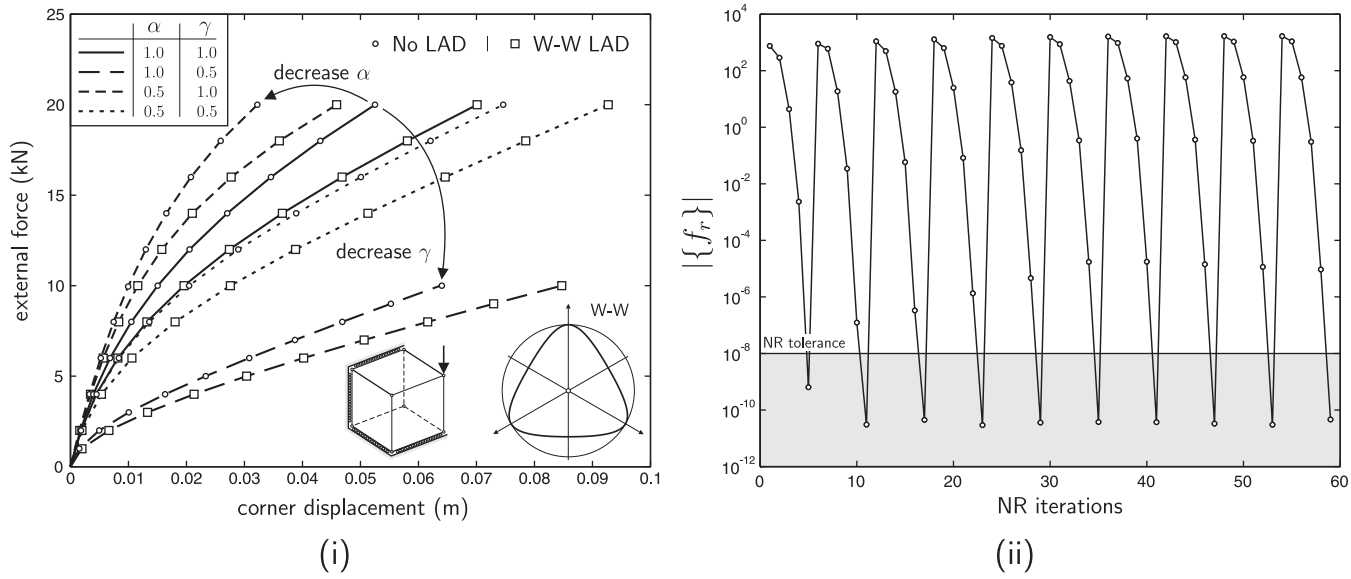

Fig. 20. Single 3D finite element analysis results (i) force–displacement plots for different forms of the model, with and without LAD (ii) convergence for the W–W LAD ($\alpha = \gamma = 0.5$).

100 kPa. Subsequently, a compressive vertical point load of 20 kN (or 10 kN for the $\alpha = 1$, $\gamma = 0.5$ model) was applied to the element's unconstrained top corner (see diagram lower centre of Fig. 20(i)), via 10 equal loadsteps. A reference pressure of 100 kPa, compressibility index of $\kappa = 0.01$, initial elastic volumetric strain $\varepsilon^e_{v0} = 0$ and a shear modulus of $G = 5$ MPa were used for the material's elastic properties. $p_c = 100$ kPa, $M = 1$, $\lambda = 0.1$ and $\bar{\rho}_e = 0.7$ define the yield surface.

Fig. 20 (i) gives the force–displacement response for the models with no LAD and with the W-W LAD. Four combinations of α and γ were investigated with the two parameters taking values of 0.5 or *1* (the yield surfaces with the W–W LAD can be seen in Fig. 7). In all cases the models with a W-W LAD produced softer results due to those envelopes being enclosed within the deviatorically circular non-LAD surfaces (that is, plastic straining started earlier in the LAD models). Due to the material being normally consolidated, with all stress points starting on the compressive nose of the yield surface, changing the values of α and γ led to a significant effect on the load–displacement response. As shown in Fig. 2, decreasing α and γ had the effect of increasing and decreasing the deviatoric yield stress (for $p > \gamma p_c/2$), respectively. This led to a stiffening up (for decreasing α) or softening down (decreasing γ) of the load–displacement response.

Fig. 20(ii) shows the N-R convergence rate for the simulation with $\alpha = \gamma = 0.5$ and the W–W LAD dependency. This figure demonstrates the asymptotic quadratic convergence of the procedure. The following measure of (residual) out-of-balance force

$$|\{f_r\}| = \sqrt{\{\{f_{ext}\} - \{f_{int}\}\}^T \{\{f_{ext}\} - \{f_{int}\}\}} \tag{74}$$

was used to determine convergence, where $\{f_{ext}\}$ and $\{f_{int}\}$ are the external and internal forces, respectively. $|\{f_r\}|$ for loadsteps 6–10 are given in Table 3.

5.5. Numerical verification: plane strain flexible footing analysis

Borja and Tamagnini [3] presented the small strain and finite deformation analysis of a 4 m flexible footing using the MCC constitutive model (with identical elasticity and hardening laws as adopted in this paper). While that analysis provides a rather simplified finite element simulation, it offers a useful comparison with which to validate the finite element framework and constitutive model described in this paper. Due to symmetry, only half of the domain (of width $2W = 40$ m, depth $H = 5$ m and footing half width b of 2 m) was discretised using 91 nine-noded plane strain quadrilateral elements with nine-point Gaussian quadrature (as shown in Fig. 21). This is the same structured mesh as used by Borja and Tamagnini [3]. The MCC constitutive model used the following parameters: $M = 0.857$, $\kappa = 0.0177$, $\lambda = 0.115$, $\bar{\rho}_e = 1.0$ and $G = 5.4$ MPa.

Table 3
Normalised residual out of balance force $|\{f_r\}|$ values for the final 5 steps of the single 3D finite element simulation with the W–W LAD ($\alpha = \gamma = 0.5$).

Iteration	Loadstep				
	6	7	8	9	10
1	1.5414e+03	1.6129e+03	1.6521e+03	1.6667e+03	1.6642e+03
2	8.6364e+02	9.5251e+02	1.0205e+03	1.0659e+03	1.0894e+03
3	4.3344e+01	5.3360e+0	5.7849e+01	5.8497e+01	5.7817e+01
4	3.4309e−01	3.9938e−01	3.6357e−01	3.3166e−01	3.0497e−01
5	1.7303e−05	1.7602e−05	1.4240e−05	1.1491e−05	9.3213e−06
6	3.7738e−ll	3.6956e−ll	3.3056e−ll	3.0253e−ll	4.6145e−ll

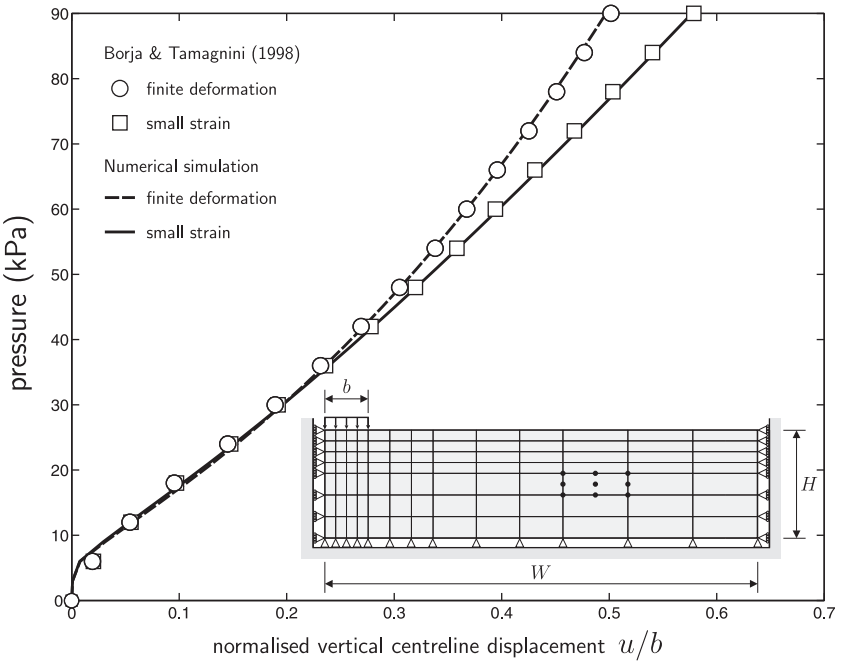

Fig. 21. Flexible footing analysis: comparison between the MCC model's pressure-centreline displacement (u) response from Borja and Tamagnini [3] (shown by discrete points) and that obtained from the analysis framework used in this paper.

The two-parameter model (of which MCC is a special case) was implemented within a Lagrangian finite deformation finite element code. The use of a logarithmic strain-Kirchhoff stress formulation, combined with an exponential map of the plastic flow, allows the incorporation of existing small strain constitutive algorithms without modification. See [16] and the references contained within for more details on the finite deformation formulation. Borja and Tamagnini [3] derived the following relationship between the small strain (Cauchy) and finite deformation (Kirchhoff) compressibility indices

$$\tilde{\kappa}_{fd} = \frac{\kappa}{1-\kappa} \quad \text{and} \quad \tilde{\lambda}_{fd} = \frac{\lambda}{1-\lambda}, \tag{75}$$

where $(\tilde{\cdot}_{fd})$ identify the finite deformation parameters. These relationships should be used to obtain the compressibility indices appropriate for finite deformation analysis based on a logarithmic strain-Kirchhoff stress formulation, as used in the recent paper by Yamakawa et al. [44].

The drained finite element simulation started from an initial overconsolidated state generated using the following small strain numerical procedure:

1. apply gravitational loads corresponding to a saturated weight of 10 kN/m^3 assuming a reference pressure p_r = 1 kPa,
2. impose a uniform surface surcharge of 5 kPa, then
3. remove the surface surcharge.

The initial elastic strains $\{\varepsilon^e\}$ and the size of the yield surface p_c for the flexible footing analysis were set equal to those obtained from the above procedure. The nodal displacements were reset to zero for the finite deformation analysis and the elastic volumetric strains increased by $\tilde{\kappa} \times \varepsilon_v^e$ to account for the change in κ between Cauchy and Kirchhoff stresses. A vertical pressure of 90 kPa was applied over the half-width of 2 m in 90 equal loadsteps.

The pressure-centreline displacement response is shown in Fig. 21. The finite element response shows excellent agreement with the results presented by Borja and Tamagnini [3] (shown by discrete points). This analysis verifies the numerical procedure for both the implemented constitutive model and the finite deformation framework.

5.6. Plane strain rigid footing analysis

A plane strain incremental small strain finite element analysis of a 1 m wide rigid strip footing bearing onto a weightless soil was performed to assess the model's performance within a more complex finite element problem. Due to symmetry, only one half of the problem was considered. The same finite element discretisation as presented in [18] was used. The mesh had a depth and

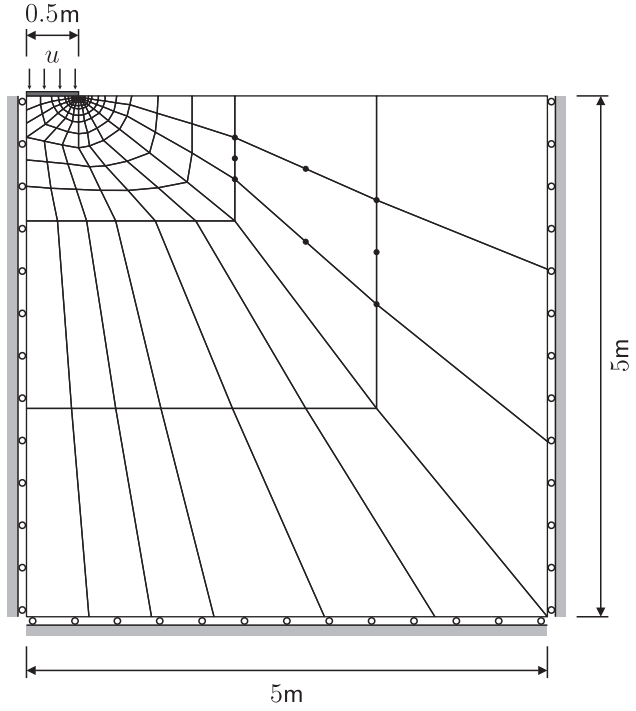

Fig. 22. Rigid strip footing plane-strain finite element discretisation.

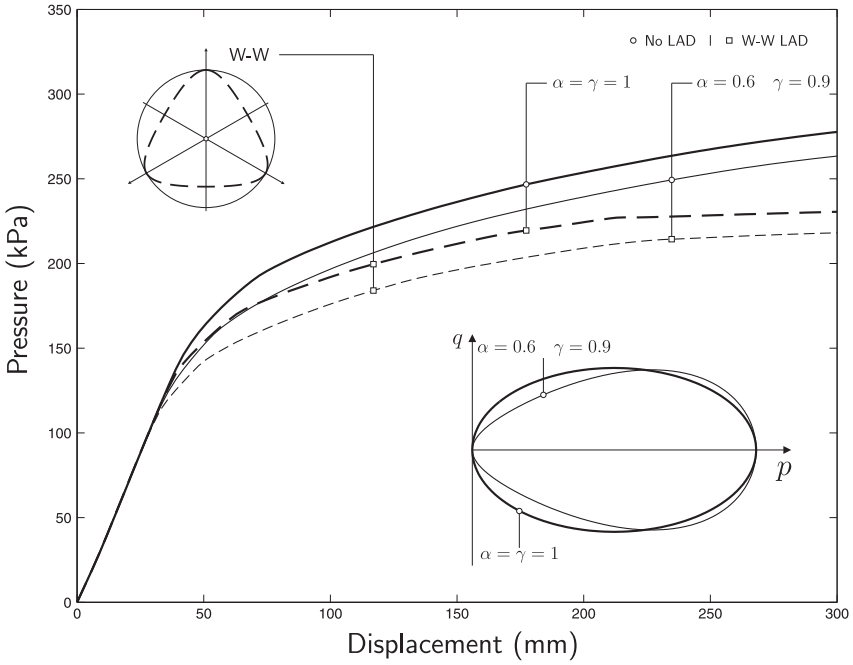

Fig. 23. Rigid strip footing pressure–displacement response.

width of 5 m (see Fig. 22). 135 eight-noded quadrilaterals, with reduced four-point quadrature, modelled the problem. The footing was assumed to be rigid and smooth with an imposed vertical displacement of 300 mm, supplied via 100 equal increments. A reference pressure of 100 kPa, compressibility index of $\kappa = 0.0322$, initial elastic volumetric strain $\varepsilon^{e}_{v0} = 0$ and a shear modulus of $G = 2.329$ MPa were used for the material's elastic properties. $p_c = 400$ kPa, $M = 0.3640$, $\lambda = 0.161$ and $\bar{\rho}_e = 0.7953$ ($\phi = 20°$) define the yield surface. Four yield surfaces were investigated: $\alpha = \gamma = 1$ and $\alpha = 0.6$, $\gamma = 0.9$ with and without a W–W LAD. Fig. 23 presents the pressure–displacement response of the footing for the four constitutive models. Reducing α and γ leads to a softer response, as does introduction of the LAD. The load required to obtain a displacement of 300 mm reduced by 87.8% for both the MCC and $\alpha = 0.6$, $\gamma = 0.9$ models.

The convergence of the footing problem for $\alpha = 0.6$, $\gamma = 0.9$ with the W–W LAD is presented in Fig. 24 for displacements 30, 60, 150, 240 and 300 mm. The out-of-balance force was determined using (74), normalised with respect to the norm of the external force vector, with a tolerance of 10^{-9}. Despite the imposed relatively large displacement increments, the convergence analysis demonstrates the robustness and efficiency of the global Newton–Raphson solution scheme when using the algorithmic consistent tangent. The number of elasto-plastic Gauss points (n_{pgp}) is also given for each displacement. The progressive development of plasticity is evident from these values.

5.7. Finite deformation cavity expansion

The final example is an analysis of the expansion of a cylindrical cavity under internal pressure. Although this is a one-dimensional axi-symmetric problem, we treat the expansion as a 2D plane strain finite element analysis. Only 3° of the domain (with a cavity internal radius of $a_0 = 1$ m and a fixed outer boundary of radius $b_0 = 2$ km) is discretised using 150 four-noded plane strain fully integrated quadrilateral elements. The size of the elements were progressively increased by a factor 1.1 from the inner to the outer surface. The internal radius (a) was expanded to 5 m via 200 equal displacement-controlled increments. In [16] this discretisation was shown to provide excellent agreement with the finite deformation analytical solution for Mohr–Coulomb.

A reference pressure of 100 kPa, compressibility index of $\tilde{\kappa} = 0.0322$, initial elastic volumetric strain $\varepsilon^{e}_{v0} = 0$ and a shear modulus of $G = 2.329$ MPa were used for the material's elastic properties. $p_c = 600$ kPa, $M = 0.4235$, $\tilde{\lambda} = 0.161$ and $\bar{\rho}_e = 0.7695$ ($\phi = 23°$) define the yield surface for this simulation.

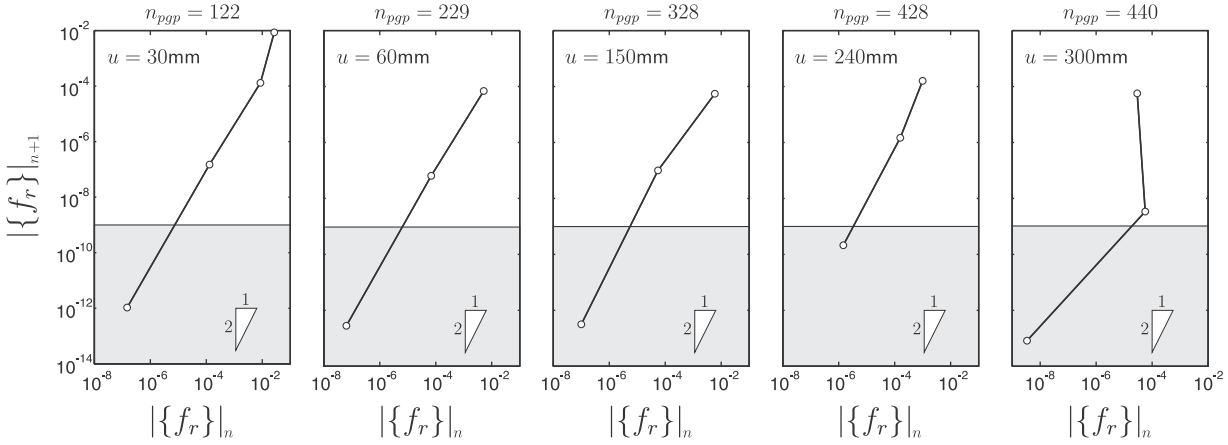

Fig. 24. Rigid strip footing convergence showing the norm of the residual out-of-balance force against the previous out-of-balance force for loadsteps 10, 20, 50, 80 and 100.

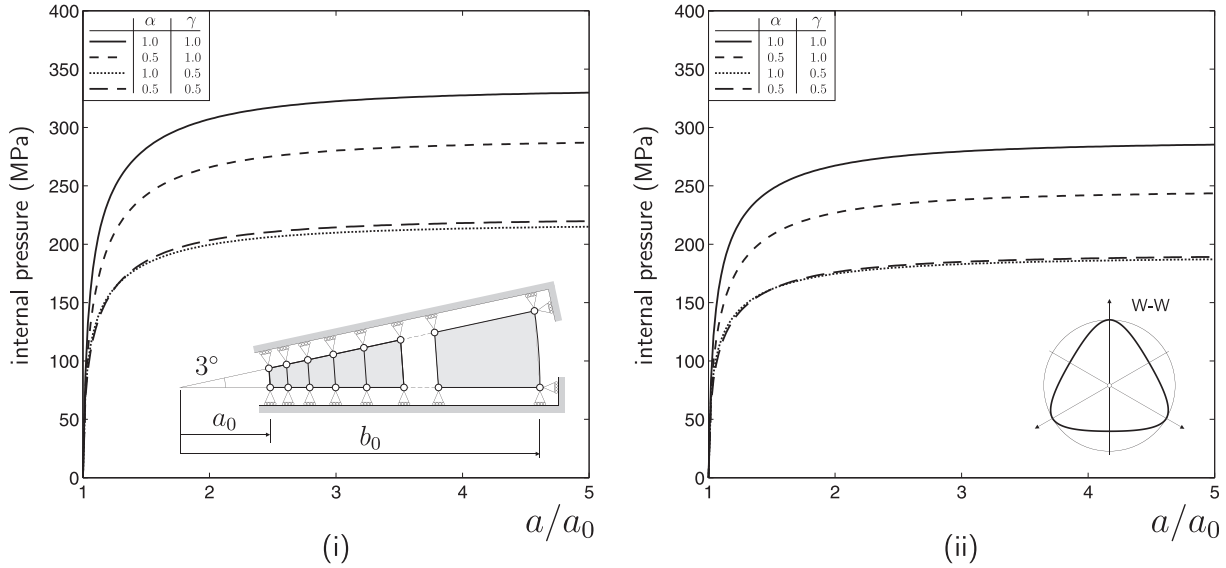

Fig. 25. Finite deformation expansion of a cylindrical cavity (i) no LAD (ii) W–W LAD with $\bar{\rho}_e = 0.7695$.

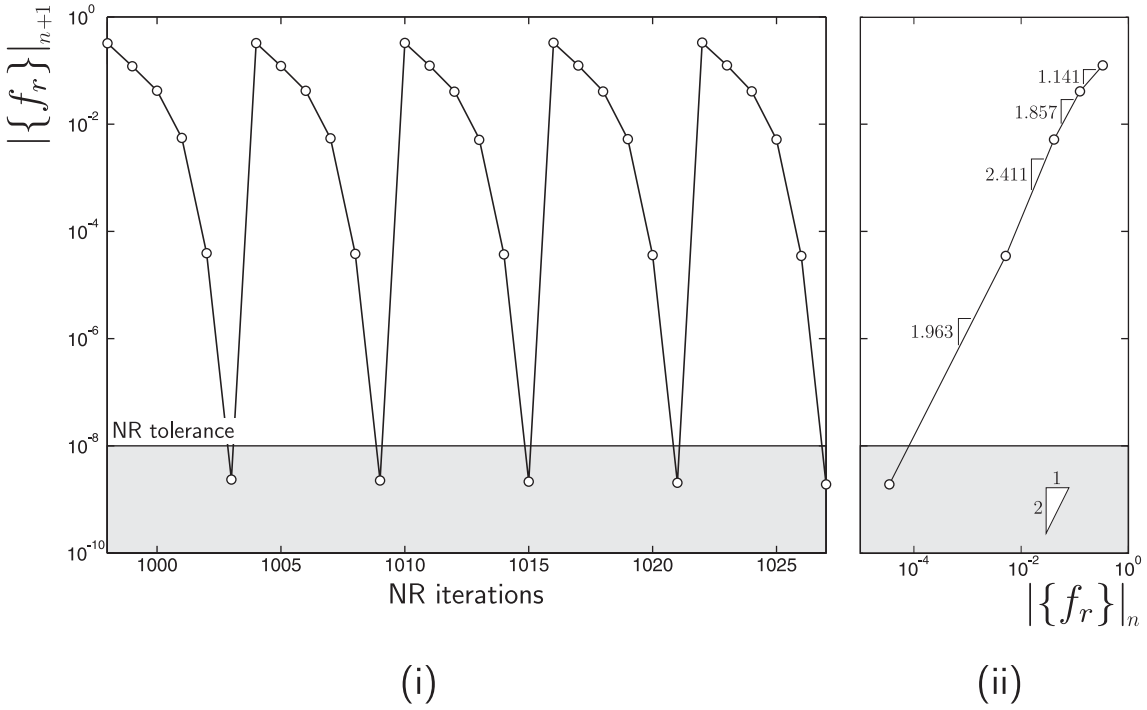

Fig. 26. Convergence results for the finite deformation expansion of a cylindrical cavity when $\alpha = 0.5$ and $\gamma = 1$ with W–W LAD: (i) norm of the residual out-of-balance force for the final five loadsteps (ii) norm of the residual out-of-balance force against the previous out-of-balance force for the final loadstep.

Fig. 25 presents the internal pressure–displacement results for the same combination of constitutive models as analyzed in Section 5.4. Fig. 25(i) and (ii) shown the results for the models with circular deviatoric sections and those with a W–W LAD, respectively. The W–W models have peak loads, on average, 86.1% lower than those seen in the models which are independent of the third invariant of stress.

Fig. 26(i) presents the convergence results for the final 5 loadsteps of the simulation with $\alpha = 0.5$, $\gamma = 1$ and a W–W LAD. This figure demonstrates the asymptotic quadratic convergence of the global finite deformation N–R procedure, where the measure of residual out-of-balance force is once again given by (74) normalised with respect to the norm of the external force vector. The convergence for the final loadstep is given in Fig. 26(ii) where the norm of the residual out-of-balance force is plotted against the previous out-of-balance force. The gradient of this line indicates the convergence rate. The results demonstrate (for this case) super-quadratic convergence until the machine precision limit is attained.

6. Conclusion

In this paper we have presented for the first time the complete backward Euler stress integration expressions and consistent tangent for the Collins and Hilder family of *two-parameter* hyperplastic Critical State constitutive models. The study includes incorporation of the elliptic Willam–Warnke Lode angle dependency on deviatoric yielding rather than the Matsuoka–Nakai LAD, as the latter can led to convergence difficulties under generalised stress increments (specifically, problems are introduced when any of the trial principal stresses are tensile).

After deriving all the expressions required for a material point algorithm, the performance of several variants of the family of models were examined. Drained triaxial compression simulations revealed improved realism over the modified Cam–Clay model for both normally and heavily over-consolidated states. Gudehus strain probe investigations provided a greater understanding of stored and dissipated plastic work for three dimensional stress paths. The robustness of the BE stress return algorithm was demonstrated, for the first time, using a linked sequence of Gudehus plots where the constitutive model is subjected to a random path of strain probes. This provides a challenging but important test for any elasto-plasticity model, as any failure to return to the hardening/softening yield surface, when exploring the full strain space, can be identified immediately.

The influence of the yield function on the implicit stress integration procedure was examined. Three forms of f that describe the same yield surface were explored. These formulations were subjected to identical trial elastic strains and their return paths observed. The tests confirm the well-behaved robust nature of the BE stress return algorithm using the new form of the yield function $(36)_1$.

Embedding the constitutive models within a Lagrangian finite element finite deformation numerical scheme allowed more demanding analyses to be performed. In each of the 22 simulations, the use of the consistent algorithmic tangent led to rapid convergence of the global Newton–Raphson nonlinear solution scheme. In all examples, the model and finite deformation code behaved stably. Further work is now required to develop a robust two-surface anisotropic version of this attractive hyperplastic Critical State framework in order to capture inelastic orientational changes to the material fabric and reproduce hysteretic effects (in a more convincing fashion) under cyclic loading.

Appendix A

A.1. Stress derivatives

This paper is concerned with isotropic constitutive equations, thus the following derivatives need only be formed with respect to the principal stresses. The derivatives of J_2 and J_3 are given by

$$\{J_{2,\sigma}\} = \frac{\{s\}}{\rho} \quad \text{and} \quad \{J_{3,\sigma}\} = \{s_2 s_3 \quad s_1 s_3 \quad s_1 s_2\}^T + \frac{J_2}{3}\{1\} \quad \left(\text{where } \rho = (2J_2)^{1/2}\right). \tag{A.1}$$

The second derivatives are

$$[J_{3,\sigma\sigma}] = \frac{2}{3}\begin{bmatrix} s_1 & s_3 & s_2 \\ s_3 & s_2 & s_1 \\ s_2 & s_1 & s_3 \end{bmatrix} \quad \text{and} \quad [J_{2,\sigma\sigma}] = \frac{1}{3}\left(3[I] - \{1\}\{1\}^T\right). \tag{A.2}$$

Taking the partial derivative of the Lode angle (30), we obtain

$$\left\{\frac{\partial\theta}{\partial\sigma}\right\} = \frac{\sqrt{3}}{2\cos 3\theta}\underbrace{\left(J_2^{-3/2}\{J_{3,\sigma}\} - \frac{3}{2}J_3J_2^{-5/2}\{s\}\right)}_{\{\vartheta\}}. \tag{A.3}$$

When on the extension meridian ($\theta = -\pi/6$), (A.3) is indeterminate. Here l'Hôpital's rule is used to construct the derivative (with $\sigma_1 > \sigma_2 > \sigma_3$)

$$\{\theta_{,\sigma}\} = \frac{\rho}{2\sqrt{6}}[\vartheta_{,\sigma}]\{0 \quad 1 \quad -1\}^T \tag{A.4}$$

and when on the compression meridian ($\theta = \pi/6$)

$$\{\theta_{,\sigma}\} = \frac{\rho}{2\sqrt{6}}[\vartheta_{,\sigma}]\{1 \quad -1 \quad 0\}^T, \tag{A.5}$$

where the derivative of $\{\vartheta\}$, see (A.3), with respect to $\{\sigma\}$ is given by

$$[\vartheta_{,\sigma}] = -\frac{3}{2}J_2^{-5/2}\left(\{s\}\{J_{3,\sigma}\}^T + \{J_{3,\sigma}\}\{s\}^T + J_3[J_{2,\sigma\sigma}]\right) + J_2^{-3/2}[J_{3,\sigma\sigma}] + \frac{15}{4}J_3J_2^{-7/2}\{s\}\{s\}^T. \tag{A.6}$$

A.2. Stress transformation

The following relations can be used to transform between six-component and principal stress and strain space

$$\{\hat{\sigma}\} = [Q]^T\begin{Bmatrix}\{\sigma\}\\ \{0\}\end{Bmatrix}, \quad \{\hat{\varepsilon}\} = [Q]^{-1}\begin{Bmatrix}\{\varepsilon\}\\ \{0\}\end{Bmatrix} \quad \text{and} \quad [\widehat{D}] = [Q]^T[D][Q]. \tag{A.7}$$

The transformation matrix is given by

$$[Q] = \begin{bmatrix} (t_1)^2 & (t_2)^2 & (t_3)^2 & t_1t_2 & t_2t_3 & t_3t_1 \\ (t_4)^2 & (t_5)^2 & (t_6)^2 & t_4t_5 & t_5t_6 & t_6t_4 \\ (t_7)^2 & (t_8)^2 & (t_9)^2 & t_7t_8 & t_8t_9 & t_9t_7 \\ 2t_1t_4 & 2t_2t_5 & 2t_3t_6 & t_1t_5 + t_4t_2 & t_2t_6 + t_5t_3 & t_3t_4 + t_6t_1 \\ 2t_4t_7 & 2t_5t_8 & 2t_6t_9 & t_4t_8 + t_7t_5 & t_5t_9 + t_8t_6 & t_6t_7 + t_9t_4 \\ 2t_7t_1 & 2t_8t_2 & 2t_9t_3 & t_7t_2 + t_1t_8 & t_8t_3 + t_2t_9 & t_9t_1 + t_3t_7 \end{bmatrix}, \tag{A.8}$$

where the components t_i are associated with the trial elastic strain eigenvectors

$$[t] = \begin{bmatrix} t_1 & t_4 & t_7 \\ t_2 & t_5 & t_8 \\ t_3 & t_6 & t_9 \end{bmatrix}. \tag{A.9}$$

References

[1] J.P. Bardet, Lode dependences for isotropic pressure-sensitive elastoplastic materials, ASME J. Appl. Mech. 57 (1990) 498–506.
[2] S.K. Bhowmik, J.H. Long, A general formulation for the cross sections of yield surfaces in octahedral planes, in: G.N. Pande, J. Middleton (Eds.), NUMENTA 90, 1990, pp. 795–803.
[3] R.I. Borja, C. Tamagnini, Cam-clay plasticity. Part III: Extension of the infinitesimal model to include finite strains, Comput. Methods Appl. Mech. Engrg 155 (1998) 73–95.
[4] R. Butterfield, A natural compression law for soils (an advance on e-log p′), Géotechnique 29 (1979) 469–480.
[5] J. Chaboche, G. Cailletaud, Integration methods for complex plastic constitutive equations, Comput. Meth. Appl. Mech. Engrg. 133 (1996) 125–155.
[6] I.F. Collins, G.T. Houlsby, Application of thermomechanical principles to the modelling of geotechnical materials, Proc. R. Soc. Lond. A. 453 (1997) 1975–2001.
[7] I.F. Collins, P.A. Kelly, A thermomechanical analysis of a family of soil models, Géotechnique 52 (2002) 507–518.
[8] I.F. Collins, T. Hilder, A theoretical framework for constructing elastic/plastic constitutive models of triaxial tests, Int. J. Numer. Methods Geomech. 26 (2002) 1313–1347.
[9] I.F. Collins, A systematic procedure for constructing critical state models in three dimensions, Int. J. Solids Struct. 40 (2003) 4379–4397.
[10] I.F. Collins, B. Muhunthan, On the relationship between stress–dilatancy, anisotropy, and plastic dissipation for granular materials, Géotechnique 53 (2003) 611–618.
[11] I.F. Collins, Elastic/plastic models for soils and sands, Int. J. Mech. Sci. 47 (2005) 493–508.
[12] I.F. Collins, The concept of stored plastic work or frozen elastic energy in soil mechanics, Géotechnique 55 (2005) 373–383.
[13] I.F. Collins, B. Muhunthan, A.T.T. Tai, J. Pender, The concept of a Reynolds–Taylor state and the mechanics of sands, Géotechnique 57 (2007) 437–447.
[14] I.F. Collins, B. Muhunthan, B. Qu, Thermomechanical state parameter models for sands, Géotechnique 60 (2010) 611–622.
[15] W.M. Coombs, R.S. Crouch, C.E. Augarde, Reuleaux plasticity: analytical backward Euler stress integration and consistent tangent, Comput. Methods Appl. Mech. Engrg. 199 (2010) 1733–1743.
[16] W.M. Coombs, R.S. Crouch, Non-associated Reuleaux plasticity: analytical stress integration and consistent tangent for finite deformation mechanics, Comput. Methods Appl. Mech. Engrg. 200 (2011) 1021–1037.
[17] Y. Dafalias, M. Manzari, A. Padadimitriou, SANICLAY: simple anisotropic clay plasticity model, Int. J. Numer. Anal. Meth. Geomech. 30 (2006) 1231–1257.
[18] E.A. de Souza Neto, D. Perić, D.R.J. Owen, Computational Methods for Plasticity: Theory and Applications, John Wiley & Sons Ltd., 2008.
[19] A. Federico, G. Elia, V. Germano, A short note on the earth pressure and mobilized angle of internal friction in one-dimensional compression of soils, J. Geoengrg. 3 (2008) 41–46.
[20] A. Gens, Stress–strain characteristics of a low plasticity clay, PhD. Thesis, Imperial College of Science and Technology, University of London, 1982.
[21] A. Gens, D. Potts, Critical state models in computational geomechanics, Engrg. Comput. 178 (1988) 178–197.
[22] K.M. Górski, E. Hivon, A.J. Banday, B.D. Wandelt, F.K. Hansen, M. Reinecke, M. Bartelmann, HEALPix: a framework for high-resolution discretization and fast analysis of data distributed on the sphere, Astrophys. J. 622 (2005) 759–771.
[23] D.V. Griffiths, Failure criteria interpretation based on Mohr–Coulomb friction, ASCE J. Geotech. Engrg. 116 (6) (1990) 986–999.
[24] G. Gudehus, Comparison of some constitutive laws for soils under radially symmetric loading and unloading, in: Proceedings of the 3rd International Conference on Numerical Methods in Geomechanics, Aachen, 1979, pp. 1309–1323.
[25] K. Hashiguchi, Verification of compatibility of isotropic consolidation characteristics of soils to multiplicative decomposition of deformation gradient, Soils Found. 48 (2008) 597–602.
[26] G. Houlsby, A study of plasticity theories and their applicability to soils, PhD. Thesis, University of Cambridge, 1981.
[27] G. Houlsby, The use of a variable shear modulus in elastic-plastic models for clays, Comput. Geotech. 1 (1985) 3–13.
[28] G. Houlsby, A. Puzrin, A thermomechanical framework for constitutive models for rate-independent dissipative materials, Int. J. Plast. 16 (2000) 1017–1047.
[29] G. Houlsby, A. Puzrin, Principles of Hyperplasticity, Springer Verlag London Limited, 2006.
[30] J. Jaky, Pressure in silos, in: Proceedings of the 2nd International Conference on Soil Mechanics and Foundation Engineering, Rotterdam, vol. 1, June 21–30, 1948, pp. 103–107.
[31] P.V. Lade, J.M. Duncan, Cubical triaxial tests on cohesionless soil, J. Soil Mech. Found. Div. ASCE (1973) 193–812.
[32] H. Matsuoka, T. Nakai, Stress-deformation and strength characteristics of soil under three different principal stresses, Proc. JSCE 232 (1974) 59–70.
[33] G.A. Maugin, The Thermomechanics of Plasticity and Fracture, Cambridge University Press, Cambridge, 1992.
[34] D. Potts, L. Zdravković, Finite Element Analysis in Geotechnical Engineering: Application, Thomas Telford Publishing, London, 2001.
[35] A. Puzrin, G. Houlsby, A thermomechanical framework for rate-independent dissipative materials with internal functions, Int. J. Plast. 17 (2001) 1147–1165.
[36] A. Puzrin, G. Houlsby, Fundamentals of kinematic hardening hyperplasticity, Int. J. Solids Struct. 38 (2001) 3771–3794.
[37] K.H. Roscoe, J.B. Burland, On the generalised stress-strain behaviour of wet clay, in: J. Heyman, F.A. Leckie (Eds.), Engineering Plasticity, Cambridge University Press, 1968, pp. 535–609.
[38] A. Schofield, P. Wroth, Critical State Soil Mechanics, McGraw-Hill Publishing Company Limited, 1968.
[39] R. Shield, On Coulomb's law of failure in soils, J. Mech. Phys. Solids 4 (1955) 10–16.
[40] J.C. Simo, R. Taylor, Consistent tangent operators for rate-independent elastoplasticity, Comput. Methosd Appl. Mech. Engrg. 48 (1985) 101–118.
[41] J.C. Simo, T.J.R. Hughes, Computational Inelasticity, Springer, New York, 1998.
[42] M. Vrh, M. Halilovič, B. Štok, Improved explicit integration in plasticity, Int. J. Numer. Methods Engrg. 81 (2010) 910–938.

[43] K.J. Willam, E.P. Warnke, Constitutive model for the triaxial behaviour of concrete, in: Proceedings of the May 17–19 1974, International Association of Bridge and Structural Engineers Seminar on Concrete Structures Subjected to Triaxial Stresses, Bergamo Italy, 1974.
[44] Y. Yamakawa, K. Hashiguchi, K. Ikeda, Implicit stress-update algorithm for isotropic Cam-clay model based on the subloading surface concept at finite strains, Int. J. Plast. 26 (2010) 634–658.
[45] H. Ziegler, An Introduction to Thermomechanics, second ed., North Holland Pub. Co, Amsterdam, 1983.
[46] M. Zytynski, M.K. Randolph, R. Nova, C.P. Wroth, On modeling the unloading–reloading behaviour of soils, Int. J. Numer. Anal. Methods Geomech. 2 (1978) 87–93.